

# Generalized Rigid and Generalized Affine Image Registration and Interpolation by Geometric Multigrid

Stephen L. Keeling\*

**Abstract.** Generalized rigid and generalized affine registration and interpolation obtained by finite displacements and by optical flow are here developed variationally and numerically as well as with respect to a geometric multigrid solution process. For high order optimality systems under natural boundary conditions, it is shown that the convergence criteria of [10] are met. Specifically, the Galerkin formalism is used together with a multi-colored ordering of unknowns to permit vectorization of a symmetric successive over-relaxation on image processing systems. The geometric multigrid procedure is situated as an inner iteration within an outer Newton or lagged diffusivity iteration, which in turn is embedded within a pyramidal scheme that initializes each outer iteration from predictions obtained on coarser levels. Differences between results obtainable by finite displacements and by optical flows are elucidated. Specifically, independence of image order can be shown for optical flow but in general not for finite displacements. Also, while autonomous optical flows are used in practice, it is shown explicitly that finite displacements generate a broader class of registrations. This work is motivated by applications in histological reconstruction and in dynamic medical imaging, and results are shown for such realistic examples.

## 1 Introduction

Separate images of related objects are compared or aligned by at least implicitly conceiving a correspondence between like points. When an explicit coordinate transformation connecting like points is constructed, images are said to be *registered*. When a parameterized transformation permits images to be morphed one to the other, images are said to be *interpolated*. In this work, a registration or interpolation method is said to be *generalized rigid* or *generalized affine* if it selects a rigid or an affine transformation respectively when one fits the given images, and otherwise the degree to which the method produces a rigid or an affine transformation can be regulated. These concepts are here formulated variationally by penalizing the departure of a transformation from being rigid or from being affine.

The motivation for considering generalizations of rigid or affine transformations lies in their applicability in two important categories of biomedical imaging. First, because of the ubiquity of rigid objects in the human body, generalized rigid registration and interpolation are of particular interest, for instance, to facilitate medical examination of dynamic imaging data particularly by increasing the temporal resolution. Secondly, generalized affine registration and interpolation are of particular interest, for instance, for object reconstruction from histological data since histological sections may be affine deformed in the process of slicing. Both of these applications are considered together in this work with respect to both finite displacements and optical flow since these concepts are so interrelated and they share so much in common in the variational and numerical formulation as well as in the geometric multigrid solution process developed here. Since both applications involve the processing of sets as opposed to pairs of images, the proposed concepts are also formulated for image sequences.

Generalized rigid registration was first considered in [21] where it was shown that that this concept is effectively limited to optical flow and that it is a more natural formulation of elastic regularization than is regularization of finite displacements by linearized elastic potential energy [8] [26]. Generalized affine registration is implemented for both optical flow and for finite displacements using second order penalties variationally [7] [27] but ultimately realized

---

\*Institut für Mathematik und Wissenschaftliches Rechnen, Karl-Franzens-Universität Graz, Heinrichstraße 36, 8010 Graz, Austria; email: stephen.keeling@uni-graz.at; tel: +43-316-380-5156; fax: +43-316-380-9815.

by employing natural boundary conditions. The combination of second order penalties together with a locally penalized departure from rigidity for finite displacements has been implemented recently in [24]. A generalized affine method is also realizable in the spline approach of [27] as well as with the diffeomorphic approach of [9], which also includes related flows as well as a multi-scale framework. In the present work, as well as in [21], it is desired to allow optical flows to be less regular and their associated registrations to be not necessarily diffeomorphic, for instance, to allow for object excision.

The consistent use of natural boundary conditions in all formulations of the present work creates a challenge for the numerical solution of discretized optimality systems as is evident from the geometric multigrid formulation developed in [20] and adapted here for image registration and interpolation problems. As pointed out in [20], algebraic multigrid is generally limited to discretizations resulting in  $M$ -matrices [28], which is not possible for the high order problems considered here. On the other hand, the geometric multigrid foundation of [10] is well suited to the problems at hand. Specifically, the Galerkin formalism is used together with a multi-colored ordering of unknowns to permit vectorization of a symmetric successive over-relaxation in systems such as MATLAB [22] or particularly in the image processing system IDL [16]. Other multigrid formulations for other registration methods have been implemented successfully [13] [12] as have fast Fourier methods [8].

It is also a priority in the present work that the image registration or interpolation result be independent of the order of two given images; see also [5], [11], [21]. Here it is seen that this goal can be achieved for optical flow but in general not for finite displacements. Another important distinction between finite displacements and optical flow is the class of registrations which can be achieved by one in relation to the other. On the basis of realistic applications it is proposed in [21] that optical flow can practically be constrained to be autonomous. However, an explicit counterexample is given here to show that the set of registrations achieved by finite displacements is indeed larger than that of those achieved by autonomous optical flows. Nevertheless, only autonomous optical flows are considered here numerically.

The paper can now be summarized as follows. In Section 2, a variational framework used throughout the paper is presented. Specifically, image similarity measures and transformation regularity measures are defined for finite displacements and for optical flow formulations. An explicit counterexample is also given here to show that the set of registrations achieved by finite displacements is indeed larger than that of those achieved by autonomous optical flows. In Section 3, optimality systems are derived for the cost functions introduced in Section 2. Also, the linear(ized) systems, which are later discretized, are shown to be well posed. At the end of Section 3, the use of these optimality systems to solve their corresponding minimization problems is summarized algorithmically. In Section 4, modifications of the results of Sections 2 and 3 are summarized for the case that sequences as opposed to pairs of images are to be registered or interpolated; see also [25]. In Section 5, the optimality systems of Section 3 are discretized numerically, including the finite element discretization whose analysis is summarized. In Section 6, a geometric multigrid formulation is presented along with the demonstration that the convergence criteria of [10] are met. Specifically, the approximation property is fulfilled through the Galerkin formalism, and the smoothing property is fulfilled by a symmetric successive over-relaxation. Section 7 is concerned with details of computational implementation and with alternative formulations. For instance, lumping of zero-order terms is beneficial in the limit of high data fidelity [19]. Also, a multi-colored ordering of unknowns is used to permit that the relaxation scheme is vectorizable in image processing systems. Challenges associated with nonlinear multigrid in the present context are illustrated in order to explain the use of linear multigrid as an inner iteration with respect to an outer quasi-Newton or lagged diffusivity iteration. Also a pyramidal scheme is described in which each outer iteration on a finer level is started by predictions obtained from a coarser level. Finally, in Section 8, the numerical methods developed and analyzed in previous sections are first applied to simple test cases, and the multigrid convergence guaranteed in Section 6 is exhibited for each registration formulation.

Then the methods are applied to realistic biomedical images to demonstrate generalized affine transformations in terms of histological reconstruction and generalized rigid transformations in terms of dynamic medical imaging.

## 2 The Variational Framework

Following the illustration in Fig. 1 for 2D images, let two given images  $I_0$  and  $I_1$  be situated

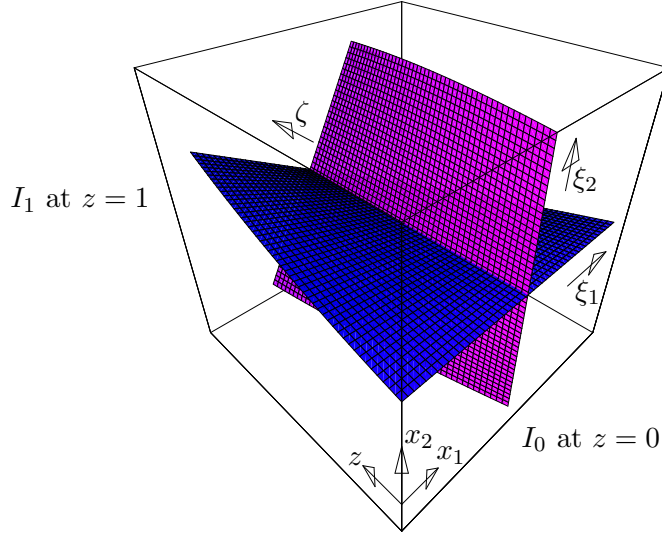


Figure 1: The domain  $Q$  with 2D images  $I_0$  and  $I_1$  on the front and back faces  $\Omega_0$  and  $\Omega_1$ , respectively. Curvilinear coordinates are defined to be constant on trajectories connecting like points in  $I_0$  and  $I_1$ .

respectively on the front and back faces,  $\Omega_0, \Omega_1 \subset \mathbf{R}^N$ , of a box,  $Q \subset \mathbf{R}^{N+1}$ , i.e.,

$$Q = \{(x_1, \dots, x_N, z) = (\mathbf{x}, z) : 0 < x_1, \dots, x_N, z < 1\} \quad (2.1)$$

$$I_0 \text{ on } \Omega_0 = \{(\mathbf{x}, z) \in \partial Q : z = 0\} \quad (2.2)$$

$$I_1 \text{ on } \Omega_1 = \{(\mathbf{x}, z) \in \partial Q : z = 1\} \quad (2.3)$$

and let  $\Omega \subset \mathbf{R}^N$  denote an otherwise generic cross section of  $Q$ . Then define curvilinear coordinates  $(\xi_1, \dots, \xi_N, \zeta) = (\boldsymbol{\xi}, \zeta)$  so that  $\boldsymbol{\xi}$  is constant along trajectories through  $Q$  that connect like points in  $I_0$  and  $I_1$ , and  $\zeta = z$ . Also, suppose that  $\mathbf{x} = \boldsymbol{\xi}$  holds in  $\Omega_0$  and therefore the displacement vector within  $Q$  is  $\mathbf{d} = \mathbf{x} - \boldsymbol{\xi}$ . Similarly define  $\boldsymbol{\eta}$  and  $\mathbf{y}$  so that  $\boldsymbol{\eta}$  is constant along trajectories together with  $\boldsymbol{\xi}$ , and  $\mathbf{y} = \boldsymbol{\eta}$  holds in  $\Omega_1$ . Further, a trajectory tangent is given by  $(u_1, \dots, u_N, 1)$  in terms of the optical flow defined as:

$$\mathbf{u} = (u_1, \dots, u_N) = \mathbf{x}_\zeta. \quad (2.4)$$

As mentioned in Section 1, for computational examples it will be assumed that the optical flow is autonomous,  $\mathbf{u}_z = 0$ .

Note that it is not assumed that every point in  $\Omega_0$  finds a like point in  $\Omega_1$ , i.e., trajectories are allowed to move out of the box  $Q$ . Let the subsets of  $\Omega_0$  and  $\Omega_1$  with respect to which trajectories extend completely through the full depth of  $Q$  be denoted respectively by  $\Omega_0^c = \{\boldsymbol{\xi} \in \Omega_0 : \mathbf{x}(\boldsymbol{\xi}, \zeta) \in Q, 0 < \zeta < 1\}$  and  $\Omega_1^c = \{\boldsymbol{\eta} \in \Omega_1 : \mathbf{y}(\boldsymbol{\eta}, \zeta) \in Q, 0 < \zeta < 1\}$ . For those trajectories extending incompletely through  $Q$  define  $\Omega_0^i = \Omega_0 \setminus \Omega_0^c$  and  $\Omega_1^i = \Omega_1 \setminus \Omega_1^c$ . Then an image similarity measure, which does not favor a given image order, is given for finite

displacements  $\mathbf{d}(\boldsymbol{\xi}, 1) = \mathbf{x}(\boldsymbol{\xi}, 1) - \boldsymbol{\xi}$  by the following sum of squared intensity differences:

$$\begin{aligned} \mathcal{S}_{\text{fd}}(\mathbf{x}) &= \int_{\Omega_0^c} [I_0(\boldsymbol{\xi}) - I_1(\mathbf{x}(\boldsymbol{\xi}))]^2 d\boldsymbol{\xi} + \int_{\Omega_1^i} [I_0(\boldsymbol{\xi}) - I_1^\infty]^2 d\boldsymbol{\xi} & (\mathbf{x}(\boldsymbol{\xi}) = \mathbf{x}(\boldsymbol{\xi}, 1)) \\ &+ \int_{\Omega_1^c} [I_0(\mathbf{y}(\boldsymbol{\eta})) - I_1(\boldsymbol{\eta})]^2 d\boldsymbol{\eta} + \int_{\Omega_1^i} [I_0^\infty - I_1(\boldsymbol{\eta})]^2 d\boldsymbol{\eta} & (\mathbf{y}(\boldsymbol{\eta}) = \mathbf{y}(\boldsymbol{\eta}, 0)) \end{aligned} \quad (2.5)$$

where  $I_0^\infty$  and  $I_1^\infty$  are the *background* intensities respectively of  $I_0$  and  $I_1$ , understood as those intensities for which no active signal is measured. These background intensities are used as though the side of the box  $Q$ ,

$$\Gamma = \partial Q \setminus \{\Omega_0 \cup \Omega_1\} \quad (2.6)$$

were not present and the trajectories impinging upon  $\Gamma$  from  $\Omega_1$  or  $\Omega_0$  would respectively be connected with  $I_0$  and  $I_1$  continued in  $\mathbf{R}^N$  by their background intensities. The measure (2.5) is equivalent to the following,

$$2 \int_{\Omega_0^c} \int_0^1 \left[ \frac{dI}{d\zeta} \right]^2 d\zeta d\boldsymbol{\xi} + \int_{\Omega_1^i} \int_0^{\zeta(\boldsymbol{\xi})} \left[ \frac{dI}{d\zeta} \right]^2 d\zeta d\boldsymbol{\xi} + \int_{\Omega_1^c} \int_{\zeta(\boldsymbol{\eta})}^1 \left[ \frac{dI}{d\zeta} \right]^2 d\zeta d\boldsymbol{\eta} \quad (2.7)$$

under the constraints [21]:

$$I(\boldsymbol{\xi}, 0) = I_0(\boldsymbol{\xi}), \quad I(\mathbf{x}(\boldsymbol{\xi}, 1), 1) = I_1(\mathbf{x}(\boldsymbol{\xi}, 1)), \quad \boldsymbol{\xi} \in \Omega_0^c \quad (2.8)$$

and

$$I(\mathbf{x}(\boldsymbol{\xi}, \zeta), \zeta) = I_1^\infty, \quad \mathbf{x}(\boldsymbol{\xi}, \zeta) \in \Gamma, \quad I(\mathbf{y}(\boldsymbol{\eta}, \zeta), \zeta) = I_0^\infty, \quad \mathbf{y}(\boldsymbol{\eta}, \zeta) \in \Gamma \quad (2.9)$$

where  $\zeta$  and  $\dot{\zeta}$ , as illustrated in Fig. 2, denote the  $\zeta$  coordinates at which trajectories emanating

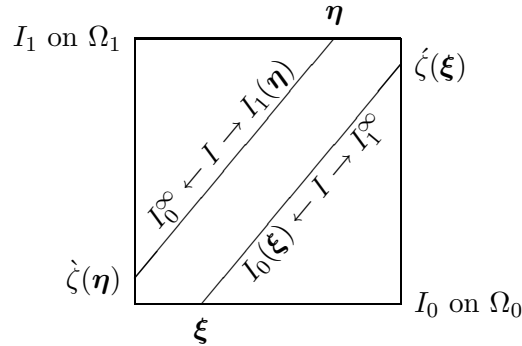


Figure 2:  $\zeta(\boldsymbol{\xi})$  and  $\zeta(\boldsymbol{\eta})$  denote the  $\zeta$  coordinates at which trajectories emanating respectively from  $\boldsymbol{\xi} \in \Omega_0^c$  and  $\boldsymbol{\eta} \in \Omega_1^i$  meet  $\Gamma$ .

respectively from  $\Omega_0^c$  and  $\Omega_1^i$  meet  $\Gamma$ . Thus,  $\dot{\zeta} = \zeta(\boldsymbol{\xi})$  and  $\dot{\zeta} = \zeta(\boldsymbol{\eta})$  are respectively defined implicitly as functions of  $\boldsymbol{\xi} \in \Omega_0^c$  and  $\boldsymbol{\eta} \in \Omega_1^i$  for (2.7).

A similarity measure which involves infinitesimal instead of finite displacements is obtained by applying the optical flow equation [15]:

$$\frac{dI}{d\zeta}(\mathbf{x}(\boldsymbol{\xi}, \zeta), \zeta) = \nabla_{\mathbf{x}} I \cdot \mathbf{x}_\zeta + I_\zeta = \nabla_{\mathbf{x}} I \cdot \mathbf{u} + I_z, \quad (2.10)$$

in (2.7) to obtain:

$$\mathcal{S}_{\text{of}}(I, \mathbf{u}) = \int_Q [\nabla_{\mathbf{x}} I \cdot \mathbf{u} + I_z]^2 d\mathbf{x} dz, \quad (2.11)$$

which has an integrand involving purely local information throughout  $Q$ . It also differs from (2.7) by not including the transformation Jacobian  $1/\det[\nabla_{\boldsymbol{\xi}} \mathbf{x}]$ . In other words, (2.11) gives a

convenient *Eulerian* (local) counterpart to the *Lagrangian* (trajectory following) form appearing in (2.7). Furthermore, the counterpart to (2.8) in the Eulerian context is given by:

$$I = I_0 \text{ on } \Omega_0, \quad I = I_1 \text{ on } \Omega_1. \quad (2.12)$$

By defining the outflow and inflow portions respectively of  $\Gamma$ ,

$$\Gamma^+ = \{(\mathbf{x}, z) \in \Gamma : \mathbf{u} \cdot \mathbf{n} > 0\}, \quad \Gamma^- = \{(\mathbf{x}, z) \in \Gamma : \mathbf{u} \cdot \mathbf{n} < 0\} \quad (2.13)$$

the counterpart to (2.9) in the Eulerian context is given by:

$$I = I_1^\infty \text{ on } \Gamma^+, \quad I = I_0^\infty \text{ on } \Gamma^-. \quad (2.14)$$

Thus, an image similarity measure is given for optical flow by (2.17) under the constraints (2.12) and (2.14).

Image registration is achieved by means of finite displacements by minimizing:

$$J_{\text{fd}}(\mathbf{x}) = \mathcal{S}_{\text{fd}}(\mathbf{x}) + \mathcal{R}_{\text{fd}}(\mathbf{x}) \quad (2.15)$$

where the similarity measure  $\mathcal{S}_{\text{fd}}$  is given in (2.5) with the notations  $\mathbf{x}(\boldsymbol{\xi})$  and  $\mathbf{y}(\boldsymbol{\eta})$  used in the context of finite displacements since the alternative notations  $\mathbf{x}(\boldsymbol{\xi}, 1)$  and  $\mathbf{y}(\boldsymbol{\eta}, 0)$  refer to trajectories. Also, the regularity measure  $\mathcal{R}_{\text{fd}}$  is defined by:

$$\mathcal{R}_{\text{fd}}(\mathbf{x}) = \mu \sum_{|\alpha|=2} \frac{2!}{\alpha!} \int_{\Omega_0} |\partial_{\boldsymbol{\xi}}^{\alpha} \mathbf{x}|^2 d\boldsymbol{\xi} \quad (2.16)$$

where  $2!/|\alpha|!$  is the multinomial coefficient for a multi-index  $\alpha$ . The second-order regularity measure  $\mathcal{R}_{\text{fd}}$  under natural boundary conditions provides generalized affine registration since  $J_{\text{fd}}$  vanishes for images related by an affine transformation. As shown in [21], generalized rigid registration is effectively ruled out for finite displacements. Note that in order for  $J_{\text{rd}}$  to be defined with the same symmetry as  $\mathcal{S}_{\text{fd}}$ , an additional term  $\mathcal{R}_{\text{fd}}(\mathbf{y})$  penalizing  $\mathbf{y} = \mathbf{x}^{-1}$  over  $\Omega_1$  exactly as  $\mathbf{x}$  is penalized over  $\Omega_0$  in  $\mathcal{R}_{\text{fd}}(\mathbf{x})$  may be added to  $J_{\text{fd}}$  with considerable cost in complexity of the formulation.

Image registration and interpolation are achieved by means of optical flow by minimizing [21]:

$$J_{\text{of},i}(I, \mathbf{u}) = \mathcal{S}_{\text{of}}(I, \mathbf{u}) + \mathcal{R}_{\text{of},i}(\mathbf{u}), \quad i = 1, 2 \quad (2.17)$$

subject to (2.12) and (2.14), where the similarity measure  $\mathcal{S}_{\text{of}}$  is given in (2.11). Under natural boundary conditions the regularity measure  $\mathcal{R}_{\text{of},i}$  can be defined as:

$$\mathcal{R}_{\text{of},1}(\mathbf{u}) = \int_Q \left[ \phi(|\nabla \mathbf{u}^T + \nabla \mathbf{u}|^2) + \gamma |\mathbf{u}_z|^2 \right] d\mathbf{x} dz. \quad (2.18)$$

for generalized rigid registration and as:

$$\mathcal{R}_{\text{of},2}(\mathbf{u}) = \int_Q \left[ \mu \sum_{\substack{|\alpha|=2 \\ \alpha_{N+1}=0}} \frac{2!}{\alpha!} |\partial_{\mathbf{x}}^{\alpha} \mathbf{u}|^2 + \gamma |\mathbf{u}_z|^2 \right] d\mathbf{x} dz \quad (2.19)$$

for generalized affine registration, since  $J_{\text{of},1}$  vanishes for images related by a rigid transformation and  $J_{\text{of},2}$  vanishes for images related by an affine transformation. In (2.18),  $|\nabla \mathbf{u}|^2 = \nabla \mathbf{u} : \nabla \mathbf{u}$  and  $:$  denotes a componentwise matrix scalar product. Also  $\phi(s) = \sqrt{s}$  for total variation regularization which is appropriate for object excision, and  $\phi(s) = s$  for Gaussian regularization which is appropriate for smoother regularizations [21]. Trajectories through the domain  $Q$  are defined by integrating the optical flow under boundary conditions, i.e., by solving:

$$\mathbf{x}(\boldsymbol{\xi}, \zeta) = \boldsymbol{\xi} + \int_0^{\zeta} \mathbf{u}(\mathbf{x}(\boldsymbol{\xi}, \rho), \rho) d\rho, \quad \boldsymbol{\xi} \in \Omega_0, \quad \zeta \in [0, 1] \quad (2.20)$$

and

$$\mathbf{y}(\boldsymbol{\eta}, \zeta) = \boldsymbol{\eta} + \int_{\zeta}^1 \mathbf{u}(\mathbf{y}(\boldsymbol{\eta}, \rho), \rho) d\rho, \quad \boldsymbol{\eta} \in \Omega_1, \quad \zeta \in [0, 1]. \quad (2.21)$$

A registration is given by the coordinate transformation  $\mathbf{x}(\boldsymbol{\xi}, 1)$  and by the inverse transformation  $\mathbf{y}(\boldsymbol{\eta}, 0)$ . The given images  $I_0$  and  $I_1$  are interpolated by the intensity  $I$ .

The fact that the regularity measure (2.18) provides generalized rigid registration and interpolation is established in [21]. That (2.19) provides generalized affine registration and interpolation can be established as follows. Note that with  $\mathbf{x}_{\zeta}(\boldsymbol{\xi}, \zeta) = \mathbf{u}(\mathbf{x}(\boldsymbol{\xi}, \zeta), \zeta)$  and  $\mathcal{R}_{\text{of},2}(\mathbf{u}) = 0$  it follows that:

$$\partial_{\zeta} \partial_{\boldsymbol{\xi}}^{\alpha} \mathbf{x} = \partial_{\boldsymbol{\xi}}^{\alpha} \mathbf{u} = \nabla_{\mathbf{x}} \mathbf{u} \partial_{\boldsymbol{\xi}}^{\alpha} \mathbf{x}, \quad |\alpha| = 2. \quad (2.22)$$

Since  $\mathbf{x}(\boldsymbol{\xi}, 0) = \boldsymbol{\xi}$  implies  $\partial_{\boldsymbol{\xi}}^{\alpha} \mathbf{x} = 0$ ,  $|\alpha| = 2$ , for  $\zeta = 0$ , it follows with (2.22) that the transformation  $\boldsymbol{\xi} \rightarrow \mathbf{x}(\boldsymbol{\xi}, \zeta)$  is affine for all  $\zeta \in [0, 1]$ .

As explained in [21], computational experiments indicate that in practice the optical flow can as well be chosen to be autonomous. On the other hand, the following example shows now that there is indeed a theoretical difference between the autonomous and nonautonomous cases of  $\gamma = \infty$  and  $\gamma < \infty$  respectively; see [4] for a related example. The nonautonomous flow,

$$\begin{aligned} x_1(\xi_1, \xi_2, \zeta) &= \frac{1}{2} + (\xi_1 - \frac{1}{2}) \cos[(\pi + \varepsilon(\xi_2 - \frac{1}{2})^2)\zeta] + (\xi_2 - \frac{1}{2}) \sin[(\pi + \varepsilon(\xi_2 - \frac{1}{2})^2)\zeta] \\ x_2(\xi_1, \xi_2, \zeta) &= \frac{1}{2} - (\xi_1 - \frac{1}{2}) \sin[(\pi + \varepsilon(\xi_2 - \frac{1}{2})^2)\zeta] + (\xi_2 - \frac{1}{2}) \cos[(\pi + \varepsilon(\xi_2 - \frac{1}{2})^2)\zeta] \end{aligned} \quad (2.23)$$

is diffeomorphic for  $\varepsilon$  sufficiently small,  $\det[\partial \mathbf{x} / \partial \boldsymbol{\xi}] = 1 - 2\varepsilon \zeta \Pi_i(\xi_i - \frac{1}{2}) > 0$ , and preserves circles,  $\sum_i (x_1 - \frac{1}{2})^2 = \sum_i (\xi_1 - \frac{1}{2})^2$ . Also, the flow manifests the following very limited periodicity with respect to the axis,  $\Xi_1 = \{\boldsymbol{\xi} : \xi_2 = \frac{1}{2}\}$ , as can be visualized in Fig. 3. The discrete map

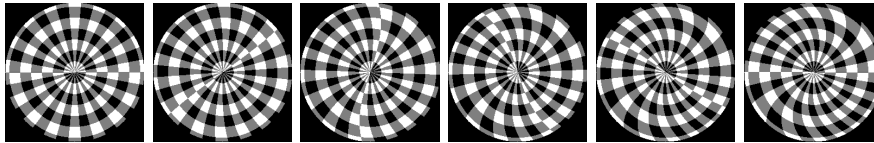


Figure 3: The two given images  $I_0$  and  $I_1$  are shown on the left and on the right. The sequence of images, read from left to right, has been determined by minimizing  $\mathcal{S}_{\text{of}}(\mathbf{u}, I) + \mathcal{R}_{\text{of},1}(\mathbf{u})$ .

$\boldsymbol{\xi} \rightarrow \mathbf{x}(\boldsymbol{\xi}, 1)$  returns  $\Xi_1$  when twice iterated,  $\mathbf{x}(\boldsymbol{\xi}_1, 2) \equiv \mathbf{x}(\mathbf{x}(\boldsymbol{\xi}_1, 1), 1) = \mathbf{x}(\boldsymbol{\xi}_1, 1) = \boldsymbol{\xi}_1$ ,  $\boldsymbol{\xi}_1 \in \Xi_1$ , but otherwise it holds that  $\mathbf{x}(\boldsymbol{\xi}, 2) \neq \boldsymbol{\xi}$ ,  $\boldsymbol{\xi} \notin \Xi_1$ . If any associated optical flow,  $\mathbf{u}(\mathbf{x}) = \mathbf{x}_{\zeta}$ , were autonomous,  $\mathbf{u}_z = 0$ , then for  $\boldsymbol{\xi}_1 \in \Xi_1$  it would follow from  $\mathbf{x}(\boldsymbol{\xi}_1, 2) = \mathbf{x}(\boldsymbol{\xi}_1, 0)$  that  $\mathbf{x}(\boldsymbol{\xi}_1, 2 + \zeta) = \mathbf{x}(\boldsymbol{\xi}_1, \zeta)$  [4]. When this equality is combined with  $\mathbf{x}(\mathbf{x}(\boldsymbol{\xi}_1, \zeta), 2) = \mathbf{x}(\boldsymbol{\xi}_1, 2 + \zeta)$ , a consequence of the uniqueness of solutions to  $\mathbf{x}_{\zeta} = \mathbf{u}(\mathbf{x})$  [4], the result with  $\boldsymbol{\xi}_0 = \mathbf{x}(\boldsymbol{\xi}_1, \zeta)$  is  $\mathbf{x}(\boldsymbol{\xi}_0, 2) = \boldsymbol{\xi}_0$ . However, the last equation cannot hold when  $\zeta$  is chosen so that  $\boldsymbol{\xi}_0 \notin \Xi_1$ . Since  $\mathbf{x}(\boldsymbol{\xi}, 1)$  is essentially determined by  $I_0(\boldsymbol{\xi}) = I_1(\mathbf{x}(\boldsymbol{\xi}, 1))$  for the strategically constructed images  $I_0$  and  $I_1$  shown respectively on the left and on the right of Fig. 3, these images cannot be interpolated or registered by an autonomous optical flow. The sequence of images shown in Fig. 3 has been determined by minimizing  $J_{\text{of},1}$  for  $\gamma < \infty$  while no such result is possible with  $\gamma = \infty$ . Nevertheless, as mentioned above, it is found in practice that the optical flow can as well be chosen to be autonomous, and autonomous flows are the focus for the computational examples of Section 8.

### 3 Optimality Conditions

In this section, the necessary optimality conditions for the variables of  $J_{\text{fd}}$  and  $J_{\text{of},i}$  are derived. As discussed in detail in Section 5, the intent is to solve cyclically for one variable with the others held fixed. Here, and throughout the paper, for a sufficiently regular domain

$D \subset \mathbf{R}^m$ , let  $C^\nu(D, \mathbf{R}^n)$  denote the Banach space of functions mapping  $D$  into  $\mathbf{R}^n$  with continuous derivatives up to order  $\nu$ . Also  $L^p(D, \mathbf{R}^n)$  denotes the Banach space of Lebesgue measurable functions from  $D$  into  $\mathbf{R}^n$  with integrable  $p$ th power while essentially bounded Lebesgue measurable functions are denoted by  $L^\infty(D, \mathbf{R}^n)$ . Then  $W^{p,\nu}(D, \mathbf{R}^n)$  denotes the Sobolev space of functions with derivatives up to order  $\nu$  in  $L^p(D, \mathbf{R}^n)$  while  $H^\nu(D, \mathbf{R}^n) = W^{2,\nu}(D, \mathbf{R}^n)$ . The usual norms, semi-norms and inner products on these spaces are denoted by  $\|\cdot\|_{W^{p,\nu}(D, \mathbf{R}^n)}$ ,  $|\cdot|_{W^{p,\nu}(D, \mathbf{R}^n)}$  and  $(\cdot, \cdot)_{H^\nu(D, \mathbf{R}^n)}$ . See [1] for further details of these function spaces.

The cost  $J_{\text{fd}}$  is stationary in the displacement when  $\mathbf{x}$  satisfies:

$$0 = \frac{1}{2} \frac{\delta J_{\text{fd}}}{\delta \mathbf{x}}(\mathbf{x}, \bar{\mathbf{x}}) = B_{\text{fd}}(\mathbf{x}, \bar{\mathbf{x}}) - F_{\text{fd}}(\mathbf{x}, \bar{\mathbf{x}}), \quad \forall \bar{\mathbf{x}} \in H^2(\Omega, \mathbf{R}^N) \quad (3.1)$$

where  $B_{\text{fd}}$  and  $F_{\text{fd}}$  are defined by:

$$B_{\text{fd}}(\mathbf{x}, \bar{\mathbf{x}}) = \mu \sum_{|\alpha|=2} \frac{2!}{\alpha!} \int_{\Omega_0} [\partial_{\xi}^{\alpha} \mathbf{x}] \cdot [\partial_{\xi}^{\alpha} \bar{\mathbf{x}}] d\xi \quad (3.2)$$

$$\begin{aligned} F_{\text{fd}}(\mathbf{x}, \bar{\mathbf{x}}) &= \int_{\Omega_0^c} [I_0(\xi) - I_1(\mathbf{x}(\xi))] \nabla_{\mathbf{x}} I_1(\mathbf{x}(\xi))^T \bar{\mathbf{x}}(\xi) d\xi \\ &+ \int_{\Omega_1^c} [I_0(\mathbf{y}(\eta)) - I_1(\eta)] \nabla_{\mathbf{y}} I_0(\mathbf{y}(\eta))^T \nabla_{\eta} \mathbf{y}(\eta) \bar{\mathbf{x}}(\mathbf{y}(\eta)) d\eta. \end{aligned} \quad (3.3)$$

The derivation of  $B_{\text{fd}} = \frac{1}{2} \delta \mathcal{R}_{\text{fd}} / \delta \mathbf{x}$  in (3.2) is standard, and  $F_{\text{fd}} = -\frac{1}{2} \delta \mathcal{S}_{\text{fd}} / \delta \mathbf{x}$  in (3.3) is derived by extending  $I_0$  and  $I_1$  outside  $\Omega_0$  and  $\Omega_1$  by their background intensities and assuming (based, e.g., on multilinear interpolation of pixel values) that the extended images are in  $W^{1,\infty}(\mathbf{R}^N, \mathbf{R})$ . Without the integrals in  $\mathcal{S}_{\text{fd}}$  which involve background intensities, the extension of images described here could not be used, and the variational derivative of  $\mathcal{S}_{\text{fd}}$  would necessarily reflect the dependence of the domains  $\Omega_0^i$  and  $\Omega_1^i$  on the displacement. Now, the variational derivative of the first line in (2.5) is computed as follows:

$$\begin{aligned} &\frac{1}{2} \frac{\delta}{\delta \mathbf{x}} \left[ \int_{\Omega_0^c} [I_0(\xi) - I_1(\mathbf{x}(\xi))]^2 d\xi + \int_{\Omega_0^i} [I_0(\xi) - I_1^\infty]^2 d\xi \right]_{(\mathbf{x}; \bar{\mathbf{x}})} \\ &\frac{1}{2} \frac{\delta}{\delta \mathbf{x}} \left[ \int_{\mathbf{R}^N} [I_0(\xi) - I_1(\mathbf{x}(\xi))]^2 d\xi \right]_{(\mathbf{x}; \bar{\mathbf{x}})} = - \int_{\mathbf{R}^N} [I_0(\xi) - I_1(\mathbf{x}(\xi))] \nabla_{\mathbf{x}} I_1(\mathbf{x}(\xi))^T \bar{\mathbf{x}}(\xi) d\xi \\ &= - \int_{\Omega_0^c} [I_0(\xi) - I_1(\mathbf{x}(\xi))] \nabla_{\mathbf{x}} I_1(\mathbf{x}(\xi))^T \bar{\mathbf{x}}(\xi) d\xi. \end{aligned} \quad (3.4)$$

The second line in (2.5) is differentiated as follows. For  $\mathbf{x}_\varepsilon = \mathbf{x} + \varepsilon \bar{\mathbf{x}}$ , let  $\mathbf{y}_\varepsilon = \mathbf{x}_\varepsilon^{-1}$  so that the variational derivative of  $\mathbf{y}$  with respect to  $\mathbf{x}$  is computed according to:

$$\begin{aligned} \mathbf{0} = \xi - \xi &= \frac{\mathbf{y}_\varepsilon(\mathbf{x}(\xi) + \varepsilon \bar{\mathbf{x}}(\xi)) - \mathbf{y}(\mathbf{x}(\xi))}{\varepsilon} \\ &= \lim_{\varepsilon \rightarrow 0} \frac{\mathbf{y}_\varepsilon(\mathbf{x}(\xi) + \varepsilon \bar{\mathbf{x}}(\xi)) - \mathbf{y}_\varepsilon(\mathbf{x}(\xi))}{\varepsilon} + \lim_{\varepsilon \rightarrow 0} \frac{\mathbf{y}_\varepsilon(\mathbf{x}(\xi)) - \mathbf{y}(\mathbf{x}(\xi))}{\varepsilon} \\ &= \nabla_{\mathbf{x}} \mathbf{y}(\mathbf{x}(\xi)) \bar{\mathbf{x}}(\xi) + \frac{\delta \mathbf{y}}{\delta \mathbf{x}}(\mathbf{x}(\xi); \bar{\mathbf{x}}(\xi)). \end{aligned} \quad (3.5)$$

Thus, the variational derivative of the second line of (2.5) is computed as follows:

$$\begin{aligned}
& \frac{1}{2} \frac{\delta}{\delta \mathbf{x}} \left[ \int_{\Omega_1^c} [I_0(\mathbf{y}(\boldsymbol{\eta})) - I_1(\boldsymbol{\eta})]^2 d\boldsymbol{\eta} + \int_{\Omega_1^i} [I_0^\infty - I_1(\boldsymbol{\eta})]^2 d\boldsymbol{\eta} \right]_{(\mathbf{y}=\mathbf{x}^{-1}; \bar{\mathbf{x}})} \\
&= \frac{1}{2} \frac{\delta}{\delta \mathbf{x}} \left[ \int_{\mathbf{R}^N} [I_0(\mathbf{y}(\boldsymbol{\eta})) - I_1(\boldsymbol{\eta})]^2 d\boldsymbol{\eta} \right]_{(\mathbf{y}=\mathbf{x}^{-1}; \bar{\mathbf{x}})} \\
&= \int_{\mathbf{R}^N} [I_0(\mathbf{y}(\boldsymbol{\eta})) - I_1(\boldsymbol{\eta})] \nabla_{\mathbf{y}} I_0(\mathbf{y}(\boldsymbol{\eta}))^\top \left[ \frac{\delta \mathbf{y}}{\delta \mathbf{x}}(\boldsymbol{\eta}; \bar{\mathbf{x}}) \right]_{=-\nabla_{\boldsymbol{\eta}} \mathbf{y}(\boldsymbol{\eta}) \bar{\mathbf{x}}} d\boldsymbol{\eta} \\
&= - \int_{\Omega_1^c} [I_0(\mathbf{y}(\boldsymbol{\eta})) - I_1(\boldsymbol{\eta})] \nabla_{\mathbf{y}} I_0(\mathbf{y}(\boldsymbol{\eta}))^\top \nabla_{\boldsymbol{\eta}} \mathbf{y}(\boldsymbol{\eta}) \bar{\mathbf{x}}(\mathbf{y}(\boldsymbol{\eta})) d\boldsymbol{\eta}
\end{aligned} \tag{3.6}$$

which leads to (3.3). Now, (3.1) is solved by the following quasi-Newton iteration:

$$\begin{cases} D_{\text{fd}}(\mathbf{d}\mathbf{x}_k, \mathbf{x}_k, \bar{\mathbf{x}}) &= - [B_{\text{fd}}(\mathbf{x}_k, \bar{\mathbf{x}}) - F_{\text{fd}}(\mathbf{x}_k, \bar{\mathbf{x}})], \quad \forall \bar{\mathbf{x}} \in H^2(\Omega_0, \mathbf{R}^N) \\ \mathbf{x}_{k+1} &= \mathbf{x}_k + \theta \mathbf{d}\mathbf{x}_k \end{cases} \quad k = 0, 1, 2, \dots \tag{3.7}$$

where:

$$D_{\text{fd}}(\mathbf{d}\mathbf{x}_k, \mathbf{x}_k, \bar{\mathbf{x}}) = B_{\text{fd}}(\mathbf{d}\mathbf{x}_k, \bar{\mathbf{x}}) + \int_{\Omega_0^c} [\nabla_{\mathbf{x}} I_1(\mathbf{x}_k(\boldsymbol{\xi})) \cdot \mathbf{d}\mathbf{x}_k(\boldsymbol{\xi})] [\nabla_{\mathbf{x}} I_1(\mathbf{x}_k(\boldsymbol{\xi})) \cdot \bar{\mathbf{x}}(\boldsymbol{\xi})] d\boldsymbol{\xi} \tag{3.8}$$

and  $\theta$  is chosen by a line search to minimize  $\mathcal{S}_{\text{fd}}$  [13]. Note that no additional boundary conditions are imposed by restricting the domain of the forms  $B_{\text{fd}}$ ,  $F_{\text{fd}}$  and  $D_{\text{fd}}$ , and thus natural boundary conditions hold. The solvability of (3.7) for fixed  $k$  is established in Theorem 1 below, which together with the other existence theorems below, depends upon the following lemma.

**Lemma 1** *Suppose  $X$  and  $Y$  are Hilbert spaces with  $Y$  compactly embedded in  $X$ . Further suppose that  $X$  is equipped with the norm  $\|\cdot\|_X$  and  $Y$  with the norm  $\|\cdot\|_Y = [|\cdot|_X^2 + |\cdot|_Y^2]^{1/2}$  where  $|\cdot|_Y$  is a semi-norm on  $Y$ . Suppose bilinear forms  $B_0$  and  $B_1$  are given satisfying:*

$$c_1 |y|_Y \leq B_1(y, y), \quad \forall y \in Y \tag{3.9}$$

and

$$B_0(y, y) > 0, \quad \forall y \neq 0 \quad \text{with} \quad B_1(y, y) = 0. \tag{3.10}$$

Then there exists a constant  $c$  such that  $B = B_1 + B_0$  satisfies:

$$c \|y\|_Y \leq B(y, y), \quad \forall y \in Y. \tag{3.11}$$

*Proof:* Assume there exists a sequence  $\{y_n\} \subset Y$  such that

$$\|y_n\|_Y = 1 \quad \text{while} \quad B(y_n, y_n) \rightarrow 0. \tag{3.12}$$

Since  $Y$  is compactly embedded in  $X$ , there is a subsequence  $\{y_{n_l}\}$  which converges in  $X$ . Because the seminorm  $|\cdot|_Y$  satisfies the inequality:

$$c_1 |y_n|_Y^2 \leq B_1(y_n, y_n) \leq B(y_n, y_n) \tag{3.13}$$

both terms on the right side of the following vanish:

$$\|y_{n_l} - y_{n_k}\|_Y^2 = \|y_{n_l} - y_{n_k}\|_X^2 + |y_{n_l} - y_{n_k}|_Y^2. \tag{3.14}$$

It follows that  $\{y_{n_l}\}$  is a Cauchy sequence in  $Y$  with some limit  $y^* \in Y$  which satisfies:

$$c_1 |y^*|_Y^2 \leq B(y^*, y^*) = \lim_{n_l \rightarrow 0} B(y_{n_l}, y_{n_l}) = 0. \tag{3.15}$$

Then from  $B(y^*, y^*) = 0$  it follows that  $B_0$  in (3.10) vanishes; thus,  $y^* = 0$  follows and contradicts the assumption that  $\|y_n\|_Y = 1$ . Therefore,  $B$  is coercive on  $Y$ .  $\blacksquare$

**Theorem 1** For  $\mathbf{x}_k \in H^2(\Omega_0, \mathbf{R}^N)$  and  $\mathbf{y}_k \in H^2(\Omega_1, \mathbf{R}^N)$  suppose  $\mathbf{x}_k = \mathbf{y}_k^{-1}$  on  $\Omega_0^c = \Omega_0 \cap \mathbf{y}_k(\Omega_1)$  and  $\mathbf{y}_k = \mathbf{x}_k^{-1}$  on  $\Omega_1^c = \Omega_1 \cap \mathbf{x}_k(\Omega_0)$ . Suppose that the image  $I_1 \in W^{1,\infty}(\Omega_1, \mathbf{R})$  satisfies:

$$\int_{\Omega_0^c} |\nabla_{\mathbf{x}} I_1(\mathbf{x}_k(\boldsymbol{\xi})) \cdot (\mathbf{c} + W\boldsymbol{\xi})|^2 d\boldsymbol{\xi} > 0, \text{ for all nonvanishing } \mathbf{c} \in \mathbf{R}^N, W \in \mathbf{R}^{N \times N}. \quad (3.16)$$

Then there exists a unique  $d\mathbf{x}_k \in H^2(\Omega_0, \mathbf{R}^N)$  such that (3.7) holds.

*Proof:* The claim follows from the Lax-Milgram Lemma [6] once it is shown that  $D(d\mathbf{x}, \bar{\mathbf{x}}) = D_{\text{fd}}(d\mathbf{x}, \mathbf{x}_k, \bar{\mathbf{x}})$  is bounded and coercive on  $H^2(\Omega_0, \mathbf{R}^N)$  and that  $F(\bar{\mathbf{x}}) = -B_{\text{fd}}(\mathbf{x}_k, \bar{\mathbf{x}}) + F_{\text{fd}}(\mathbf{x}_k, \bar{\mathbf{x}})$  is bounded on  $H^2(\Omega_0, \mathbf{R}^N)$ . The boundedness of  $F$  is established by estimating (3.2) and (3.3):

$$\begin{aligned} |F(\bar{\mathbf{x}})| &\leq 2\mu \|\mathbf{x}_k\|_{H^2(\Omega_0, \mathbf{R}^N)} \|\bar{\mathbf{x}}\|_{H^2(\Omega_0, \mathbf{R}^N)} \\ &+ [\|I_0\|_{L^\infty(\Omega_0, \mathbf{R})} + \|I_1\|_{L^\infty(\Omega_1, \mathbf{R})}] \|I_1\|_{W^{1,\infty}(\Omega_1, \mathbf{R})} \|\bar{\mathbf{x}}\|_{L^1(\Omega_0, \mathbf{R}^N)} \\ &+ [\|I_0\|_{L^\infty(\Omega_0, \mathbf{R})} + \|I_1\|_{L^\infty(\Omega_1, \mathbf{R})}] \|I_0\|_{W^{1,\infty}(\Omega_0, \mathbf{R})} \|\mathbf{y}_k\|_{H^1(\Omega_1, \mathbf{R}^N)} \|\bar{\mathbf{x}}\|_{L^2(\Omega_0, \mathbf{R}^N)} \\ &\leq \{2\mu \|\mathbf{x}_k\|_{H^2(\Omega_0, \mathbf{R}^N)} + [\|I_0\|_{L^\infty(\Omega_0, \mathbf{R})} + \|I_1\|_{L^\infty(\Omega_1, \mathbf{R})}] \times \\ &\quad [\|I_1\|_{W^{1,\infty}(\Omega_1, \mathbf{R})} \mu(\Omega_0) + \|I_0\|_{W^{1,\infty}(\Omega_0, \mathbf{R})} \|\mathbf{y}_k\|_{H^1(\Omega_1, \mathbf{R}^N)}]\} \|\bar{\mathbf{x}}\|_{H^2(\Omega_0, \mathbf{R}^N)}. \end{aligned} \quad (3.17)$$

The boundedness of  $D$  is readily established,

$$|D(d\mathbf{x}, \bar{\mathbf{x}})| \leq [2\mu + \|I_1\|_{W^{1,\infty}(\Omega_1, \mathbf{R})}^2] \|d\mathbf{x}\|_{H^2(\Omega_0, \mathbf{R}^N)} \|\bar{\mathbf{x}}\|_{H^2(\Omega_0, \mathbf{R}^N)} \quad (3.18)$$

and the coercivity of  $D$  on  $H^2(\Omega_0, \mathbf{R}^N)$  follows using Lemma 1.  $\blacksquare$

The similarity measure  $\mathcal{S}_{\text{of}}$  is stationary in the intensity  $I$  for fixed  $\mathbf{u}$  when  $I$  satisfies the following in terms of quantities defined below in a Lagrangian frame [21]:

$$I(\mathbf{x}(\boldsymbol{\xi}, \zeta), \zeta) = \begin{cases} I_0(\boldsymbol{\xi})[1 - U(\boldsymbol{\xi}, \zeta, 1)] + I_1(\mathbf{x}(\boldsymbol{\xi}, 1))U(\boldsymbol{\xi}, \zeta, 1), & \boldsymbol{\xi} \in \Omega_0^c \\ I_0(\boldsymbol{\xi})[1 - U(\boldsymbol{\xi}, \zeta, \zeta)] + I_1^\infty U(\boldsymbol{\xi}, \zeta, \zeta), & \mathbf{x}(\boldsymbol{\xi}, \zeta) \in \Gamma, \boldsymbol{\xi} \in \Omega_0^i \end{cases} \quad (3.19)$$

$$I(\mathbf{y}(\boldsymbol{\eta}, \zeta), \zeta) = \begin{cases} I_1(\boldsymbol{\eta})[1 - V(\boldsymbol{\eta}, 0, \zeta)] + I_0(\mathbf{y}(\boldsymbol{\eta}, 0))V(\boldsymbol{\eta}, 0, \zeta), & \boldsymbol{\eta} \in \Omega_1^c \\ I_1(\boldsymbol{\eta})[1 - V(\boldsymbol{\eta}, \zeta, \zeta)] + I_0^\infty V(\boldsymbol{\eta}, \zeta, \zeta), & \mathbf{y}(\boldsymbol{\eta}, \zeta) \in \Gamma, \boldsymbol{\eta} \in \Omega_1^i. \end{cases} \quad (3.20)$$

As illustrated in Fig. 2, the parameters  $\zeta$  and  $\check{\zeta}$  denote the  $\zeta$  coordinates at which trajectories emanating respectively from  $\Omega_0^i$  and  $\Omega_1^i$  meet  $\Gamma$ . Then, define  $U$  and  $V$  by:

$$U(\boldsymbol{\xi}, \zeta, \zeta) = \frac{\tilde{U}(\boldsymbol{\xi}, \zeta) - \tilde{U}(\boldsymbol{\xi}, 0)}{\tilde{U}(\boldsymbol{\xi}, \zeta) - \tilde{U}(\boldsymbol{\xi}, 0)}, \quad \tilde{U}(\boldsymbol{\xi}, \zeta) = \int_{\zeta_0}^{\zeta} \exp \left[ - \int_{\zeta_0}^{\rho} \nabla \cdot \mathbf{u}(\mathbf{x}(\boldsymbol{\xi}, \rho), \rho) d\rho \right] d\rho, \quad (3.21)$$

for  $\boldsymbol{\xi} \in \Omega_0$ ,  $\zeta \in [0, \zeta]$ , and arbitrary  $\zeta_0 \in [0, \zeta]$ , and:

$$V(\boldsymbol{\eta}, \zeta, \zeta) = \frac{\tilde{V}(\boldsymbol{\eta}, 1) - \tilde{V}(\boldsymbol{\eta}, \zeta)}{\tilde{V}(\boldsymbol{\eta}, 1) - \tilde{V}(\boldsymbol{\eta}, \zeta)}, \quad \tilde{V}(\boldsymbol{\eta}, \zeta) = \int_{\zeta_0}^{\zeta} \exp \left[ - \int_{\zeta_0}^{\rho} \nabla \cdot \mathbf{u}(\mathbf{y}(\boldsymbol{\eta}, \rho), \rho) d\rho \right] d\rho, \quad (3.22)$$

for  $\boldsymbol{\eta} \in \Omega_1$ ,  $\zeta \in [\check{\zeta}, 1]$ , and arbitrary  $\zeta_0 \in [\check{\zeta}, 1]$ .

The cost  $J_{\text{of},1}$  is stationary in the optical flow  $\mathbf{u}$  for fixed  $I$  when  $\mathbf{u}$  satisfies:

$$0 = \frac{1}{2} \frac{\delta J_{\text{of}}}{\delta \mathbf{u}}(\mathbf{u}, \bar{\mathbf{u}}) = B_{\text{of},1}(\mathbf{u}, \mathbf{u}, \bar{\mathbf{u}}) - F_{\text{of}}(\bar{\mathbf{u}}), \quad \forall \bar{\mathbf{u}} \in H^1(Q, \mathbf{R}^N), \quad (3.23)$$

where  $B_{\text{of},1}$  and  $F_{\text{of}}$  are defined by:

$$\begin{aligned} B_{\text{of},1}(\mathbf{u}, \mathbf{v}, \bar{\mathbf{u}}) &= \int_Q [(\nabla I \cdot \mathbf{u})(\nabla I \cdot \bar{\mathbf{u}}) + \gamma(\mathbf{u}_z \cdot \bar{\mathbf{u}}_z)] d\mathbf{x}d\mathbf{z} \\ &+ \int_Q \phi' \left( |\nabla \mathbf{v}^T + \nabla \mathbf{v}|^2 \right) (\nabla \mathbf{u}^T + \nabla \mathbf{u}) : (\nabla \bar{\mathbf{u}}^T + \nabla \bar{\mathbf{u}}) d\mathbf{x}d\mathbf{z} \end{aligned} \quad (3.24)$$

$$F_{\text{of}}(\bar{\mathbf{u}}) = - \int_Q I_z \nabla I \cdot \bar{\mathbf{u}} d\mathbf{x}d\mathbf{z}. \quad (3.25)$$

Now, (3.23) is solved by the lagged diffusivity iteration [29]:

$$B_{\text{of},1}(\mathbf{u}_k, \mathbf{u}_{k-1}, \bar{\mathbf{u}}) = F_{\text{of}}(\bar{\mathbf{u}}), \quad \forall \bar{\mathbf{u}} \in H^1(Q, \mathbf{R}^N), \quad k = 1, 2, 3, \dots \quad (3.26)$$

Note that no additional boundary conditions are imposed by restricting the domain of the form  $B_{\text{of},1}$ , and thus natural boundary conditions hold. The solvability of (3.26) is stated as follows and established in [21], with trivial modifications of the kind appearing in the proof of Theorem 3 for the autonomous case that  $\gamma = \infty$ .

**Theorem 2** *Suppose that the intensity  $I \in W^{1,\infty}(Q, \mathbf{R})$  satisfies:*

$$\int_Q |\nabla I \cdot (\mathbf{c} + W\mathbf{x})|^2 d\mathbf{x}dz > 0, \quad \begin{cases} \text{for every nonvanishing } \mathbf{c} \in \mathbf{R}^N \\ \text{and for every nonvanishing} \\ \text{skew symmetric matrix } W \in \mathbf{R}^{N \times N}. \end{cases} \quad (3.27)$$

Then with  $\phi(s) = \mu(\mathbf{x}, z)s$ ,  $0 < \mu_0 \leq \mu(\mathbf{x}, z) \leq \mu_1 < \infty$ , there exists a unique  $\mathbf{u}_k \in H^1(Q, \mathbf{R}^N)$  such that (3.26) holds. If  $\gamma = \infty$  so that the arguments of  $B_{\text{of},1}$  in (3.24) are  $z$ -independent, then (3.26) holds with  $Q$  replaced by  $\Omega$ .

It is furthermore assumed that  $\mathbf{u} \in H^1(Q, \mathbf{R}^N)$  has sufficient regularity so that (2.20) and (2.21) are well defined; see the discussion and references in [21].

The cost  $J_{\text{of},2}$  is stationary in the optical flow  $\mathbf{u}$  for fixed  $I$  when  $\mathbf{u}$  satisfies:

$$0 = \frac{1}{2} \frac{\delta J_{\text{of}}}{\delta \mathbf{u}}(\mathbf{u}, \bar{\mathbf{u}}) = B_{\text{of},2}(\mathbf{u}, \bar{\mathbf{u}}) - F_{\text{of}}(\bar{\mathbf{u}}), \quad \forall \bar{\mathbf{u}} \in \mathcal{H}^2(Q, \mathbf{R}^N), \quad (3.28)$$

where  $B_{\text{of},2}$  is defined by:

$$\begin{aligned} B_{\text{of},2}(\mathbf{u}, \bar{\mathbf{u}}) &= \int_Q [(\nabla I \cdot \mathbf{u})(\nabla I \cdot \bar{\mathbf{u}}) + \gamma(\mathbf{u}_z \cdot \bar{\mathbf{u}}_z)] d\mathbf{x}dz \\ &+ \mu \sum_{\substack{|\alpha|=2 \\ \alpha_{N+1}=0}} \frac{2!}{\alpha!} \int_Q (\partial^\alpha \mathbf{u}) \cdot (\partial^\alpha \bar{\mathbf{u}}) d\mathbf{x}dz \end{aligned} \quad (3.29)$$

$F_{\text{of}}$  is again defined by (3.25), and the Hilbert space and norm are defined according to:

$$\mathcal{H}^2(Q, \mathbf{R}^N) = \{\mathbf{u} \in H^1(Q, \mathbf{R}^N) : \partial^\alpha \mathbf{u} \in L^2(Q, \mathbf{R}^N), \quad |\alpha| = 2, \quad \alpha_{N+1} = 0\}$$

$$\|\mathbf{u}\|_{\mathcal{H}^2(Q, \mathbf{R}^N)}^2 = \|\mathbf{u}\|_{H^1(Q, \mathbf{R}^N)}^2 + \sum_{\substack{|\alpha|=2 \\ \alpha_{N+1}=0}} \int_Q |\partial^\alpha \mathbf{u}|^2 d\mathbf{x}dz. \quad (3.30)$$

Note that no additional boundary conditions are imposed by restricting the domain of the form  $B_{\text{of},2}$ , and thus natural boundary conditions hold. The solvability of (3.28) is established as follows.

**Theorem 3** *Suppose that the intensity  $I \in W^{1,\infty}(Q, \mathbf{R})$  satisfies:*

$$\int_Q |\nabla I \cdot (\mathbf{c} + W\mathbf{x})|^2 d\mathbf{x}dz > 0, \quad \text{for all nonvanishing } \mathbf{c} \in \mathbf{R}^N, W \in \mathbf{R}^{N \times N}. \quad (3.31)$$

Then there exists a unique  $\mathbf{u} \in \mathcal{H}^2(Q, \mathbf{R}^N)$  such that (3.28) holds. If  $\gamma = \infty$  so that the arguments of  $B_{\text{of},2}$  in (3.29) are  $z$ -independent, then (3.28) holds with  $Q$  replaced by  $\Omega$ .

*Proof:* Note that  $\mathcal{H}^2(Q, \mathbf{R}^N)$  is established as a Hilbert space with the same methods as the usual Sobolev spaces are. If  $\gamma = \infty$ ,  $\mathcal{H}^2(Q, \mathbf{R}^N)$  is replaced by  $H^2(\Omega, \mathbf{R}^N)$  and all norms of  $\mathbf{u}$  or  $\bar{\mathbf{u}}$  over  $Q$  are replaced by corresponding norms over  $\Omega$ . The claim follows from the Lax-Milgram Lemma [6] once it is shown that  $B_{\text{of},2}$  is bounded and coercive on  $\mathcal{H}^2(Q, \mathbf{R}^N)$  and that  $F_{\text{of}}$  is bounded on  $\mathcal{H}^2(Q, \mathbf{R}^N)$ . The boundedness of  $B_{\text{of},2}$  and  $F_{\text{of}}$  is readily established:

$$\begin{aligned} |B_{\text{of},2}(\mathbf{u}, \bar{\mathbf{u}})| &\leq \|I\|_{W^{1,\infty}(Q, \mathbf{R})}^2 \|\mathbf{u}\|_{L^2(Q, \mathbf{R}^N)} \|\bar{\mathbf{u}}\|_{L^2(Q, \mathbf{R}^N)} + \gamma \|\mathbf{u}_z\|_{L^2(Q, \mathbf{R}^N)} \|\bar{\mathbf{u}}_z\|_{L^2(Q, \mathbf{R}^N)} \\ &\quad + 2\mu \|\mathbf{u}\|_{\mathcal{H}^2(Q, \mathbf{R}^N)} \|\bar{\mathbf{u}}\|_{\mathcal{H}^2(Q, \mathbf{R}^N)} \\ &\leq [\|I\|_{W^{1,\infty}(Q, \mathbf{R})}^2 + \gamma + 2\mu] \|\mathbf{u}\|_{\mathcal{H}^2(Q, \mathbf{R}^N)} \|\bar{\mathbf{u}}\|_{\mathcal{H}^2(Q, \mathbf{R}^N)} \end{aligned} \quad (3.32)$$

$$|F_{\text{of}}(\bar{\mathbf{u}})| \leq \|I\|_{W^{1,\infty}(Q, \mathbf{R})}^2 \|\bar{\mathbf{u}}\|_{L^2(Q, \mathbf{R}^N)} \leq \|I\|_{W^{1,\infty}(Q, \mathbf{R})}^2 \|\bar{\mathbf{u}}\|_{\mathcal{H}^2(Q, \mathbf{R}^N)}. \quad (3.33)$$

The coercivity of  $B_{\text{of},2}$  on  $\mathcal{H}^2(Q, \mathbf{R}^N)$  follows using Lemma 1. ■

It is furthermore assumed that  $\mathbf{u} \in \mathcal{H}^2(Q, \mathbf{R}^N)$  has sufficient regularity so that (2.20) and (2.21) are well defined; see the discussion and references in [21].

Although (2.5) and (2.11) have been constructed with the priority that registration be independent of image order, this order independence can only be shown in general for optical flow and not for finite displacements. Specifically, suppose two one-dimensional images satisfy the following one-dimensional formulation of (3.1):

$$\mu D_\xi^4 x(\xi) + [I_1(x(\xi)) - I_0(\xi)][I_1'(x(\xi)) + I_0'(\xi)] = 0 \quad (3.34)$$

where  $D_\xi^4$  is defined with the natural boundary conditions that third and second order normal derivatives vanish on  $\partial\Omega$ . Then the following does not necessarily hold:

$$\mu D_\eta^4 y(\eta) + [I_0(y(\eta)) - I_1(\eta)][I_0'(y(\eta)) + I_1'(\eta)] = 0 \quad (3.35)$$

unless  $y = x^{-1}$  satisfies  $D_\eta^4 y(\eta) = -D_\xi^4 x(\xi)$ , which is the case for instance when the registration is affine. However, as indicated in the discussion of (2.16), when  $J_{\text{fd}}$  contains a term  $\mathcal{R}_{\text{fd}}(\mathbf{y})$  penalizing  $\mathbf{y}$  over  $\Omega_1$  exactly as  $\mathbf{x}$  is penalized over  $\Omega_0$  in  $\mathcal{R}_{\text{fd}}(\mathbf{x})$ , the asymmetry in (3.34) and (3.35) disappears, albeit with considerable cost in complexity of the formulation. On the other hand, order independence for optical flow can be seen readily by exchanging images and by replacing  $I(\mathbf{x}, z)$  and  $\mathbf{u}(\mathbf{x})$  with  $I(\mathbf{x}, 1 - z)$  and  $-\mathbf{u}(\mathbf{x})$  respectively and observing equality in (3.19), (3.20), (3.23) and (3.28) after the transformation.

The registration schemes for finite displacements and for optical flow can now be summarized algorithmically as follows.

- For finite displacements: set  $\mathbf{x}(\boldsymbol{\xi}) = \boldsymbol{\xi}$  and continue the following until changes in  $\mathbf{x}$  meet a convergence criterion:
  - solve one step of (3.7) for the solution of (3.1), and in the process,
  - perform a line search to determine the step size in (3.7) so that (2.5) is minimized.
- For optical flow: set  $\mathbf{u} = 0$  and continue the following until changes in  $\mathbf{u}$  meet a convergence criterion:
  - perform the integrations (2.20), (2.21), (3.21) and (3.22),
  - compute  $I$  from (3.19) and (3.20),
  - solve (3.28) for the optical flow, or
  - solve one step of (3.26) for the solution of (3.23), while (3.26) is equivalent to (3.23) when (3.23) is linear.

The discretization and numerical solution of these equations is detailed in Sections 5 and 6.

## 4 Processing Image Sequences

An image sequence may be registered or interpolated of course by processing the images only pairwise and concatenating the results. On the other hand, a coupling among images may be introduced as follows; see also [25].

The images of a sequence  $\{I_l\}_{l=0}^L$  can be registered simultaneously using finite displacements  $\{\mathbf{x}_l\}_{l=1}^L$  by minimizing:

$$J_{\text{fd}}^{(L)}(\mathbf{x}_1, \dots, \mathbf{x}_L) = \sum_{l=1}^L \mathcal{S}_{\text{fd}}^{(l)}(\mathbf{x}_1, \dots, \mathbf{x}_L) + \mathcal{R}_{\text{fd}}(\mathbf{x}_l) \quad (4.36)$$

where:

$$\mathcal{S}_{\text{fd}}^{(l)}(\mathbf{x}_1, \dots, \mathbf{x}_L) = \sum_{|l-j|=1} \int_{\mathbf{R}^N} [I_j(\mathbf{x}_j(\boldsymbol{\xi})) - I_l(\mathbf{x}_l(\boldsymbol{\xi}))]^2 d\boldsymbol{\xi} \quad (4.37)$$

and, as in the derivation of  $F_{\text{fd}}$ , all images are extended smoothly by their background intensities outside their domains,  $\Omega_l$ , which are defined analogously as discussed in Section 2. The end indices  $l = 0$  and  $l = L$  in (4.36) correspond to pairwise registration with the single near neighbor. When (4.36) has been minimized, the point  $\mathbf{x}_i(\boldsymbol{\xi}) \in \Omega_i$  has been matched to the point  $\mathbf{x}_j(\boldsymbol{\xi}) \in \Omega_j$ . To minimize  $J_{\text{fd}}^{(L)}$  with respect to  $\mathbf{x}_l$  while all other transformations are held fixed, replace  $F_{\text{fd}}$  in (3.1) and (3.7) with  $F_{\text{fd}}^{(l)} = -\frac{1}{2}\delta\mathcal{S}_{\text{fd}}^{(l)}/\delta\mathbf{x}$ :

$$F_{\text{fd}}^{(l)}(\mathbf{x}_l, \bar{\mathbf{x}}) = \int_{\mathbf{R}^N} \sum_{|l-j|=1} [I_j(\mathbf{x}_j(\boldsymbol{\xi})) - I_l(\mathbf{x}_l(\boldsymbol{\xi}))] \nabla_{\mathbf{x}} I_l(\mathbf{x}_l(\boldsymbol{\xi}))^T \bar{\mathbf{x}}(\boldsymbol{\xi}) d\boldsymbol{\xi}. \quad (4.38)$$

The functional of (4.36) can be minimized by freezing all current transformations except for one, minimizing the functional with respect to the selected transformation, updating that transformation immediately (Gauss-Seidel strategy) or else updating all transformations simultaneously (Jacobi strategy), and then repeating the process until the updates have converged. Known transformations can remain frozen as fixed boundary conditions, e.g., at one or both of the end indices  $l = 0$  and  $l = L$  in (4.36) when the position of one or both of the end images  $I_0$  and  $I_L$  is known.

The calculation (4.38) shows that  $J_{\text{fd}}^{(L)}$  is just as well minimized with respect to  $\mathbf{x}_l$  by registering the image  $I_l$  with the averaged image  $I_n(\boldsymbol{\xi}) = \sum_{|j-l|=1}^{0 \leq j \leq L} I_j(\mathbf{x}_j(\boldsymbol{\xi})) / \sum_{|j-l|=1}^{0 \leq j \leq L} 1$ . Analogously, the images  $\{I_l\}_{l=0}^L$  can be registered simultaneously by computing autonomous optical flows  $\{\mathbf{u}_l\}_{l=0}^L$  for the image pairs  $\{[I_l, I_n]\}_{l=0}^L$  according to the pairwise procedures of the present work, where the transformations  $\{\mathbf{x}_l\}_{l=0}^L$  are computed by using their respective flows in (2.20). Then the flows and their corresponding transformations can be updated repeatedly until convergence.

The images  $\{I_l\}_{l=0}^L$  can be interpolated from autonomous optical flows  $\{\mathbf{u}_l\}_{l=0}^{L-1+\nu}$  using the semi-discretization defined on  $Q^{(L)} = \Omega \times (0, L)$ :

$$\mathbf{u}(\mathbf{x}, z) = \sum_{l=0}^L \mathbf{u}_l(\mathbf{x}) \chi_l^\nu(z) \quad (4.39)$$

where  $\{\chi_l^\nu\}_{l=0}^{L-1+\nu}$  is a basis for the canonical B-splines of degree  $\nu$  defined on the grid  $\{[l, l+1]\}_{l=0}^{L-1}$  of  $[0, L]$  [14]. Then the transformations are given by the following modifications of (2.20) and (2.21):

$$\mathbf{x}(\boldsymbol{\xi}, \zeta) = \boldsymbol{\xi} + \int_l^\zeta \mathbf{u}(\mathbf{x}(\boldsymbol{\xi}, \rho), \rho) d\rho, \quad \boldsymbol{\xi} \in \Omega_l, \quad \zeta \in [l, l+1] \quad (4.40)$$

and

$$\mathbf{y}(\boldsymbol{\eta}, \zeta) = \boldsymbol{\eta} + \int_\zeta^{l+1} \mathbf{u}(\mathbf{y}(\boldsymbol{\eta}, \rho), \rho) d\rho, \quad \boldsymbol{\eta} \in \Omega_{l+1}, \quad \zeta \in [l, l+1] \quad (4.41)$$

and for  $\Gamma^{(L)} = \partial Q^{(L)} \setminus \{\Omega_0 \cup \Omega_L\}$  the intensity  $I$  is given by the following modifications of (3.19) and (3.20):

$$I(\mathbf{x}(\boldsymbol{\xi}, \zeta), \zeta) = \begin{cases} I_{l-1}(\boldsymbol{\xi})[1 - U(\boldsymbol{\xi}, \zeta, l+1)] + I_l(\mathbf{x}(\boldsymbol{\xi}, l+1))U(\boldsymbol{\xi}, \zeta, l+1), & \boldsymbol{\xi} \in \Omega_l^c \\ I_{l-1}(\boldsymbol{\xi})[1 - U(\boldsymbol{\xi}, \zeta, \zeta)] + I_l^\infty U(\boldsymbol{\xi}, \zeta, \zeta), & \mathbf{x}(\boldsymbol{\xi}, \zeta) \in \Gamma^{(L)}, \boldsymbol{\xi} \in \Omega_{l-1}^i \end{cases} \quad (4.42)$$

$$I(\mathbf{y}(\boldsymbol{\eta}, \zeta), \zeta) = \begin{cases} I_l(\boldsymbol{\eta})[1 - V(\boldsymbol{\eta}, l, \zeta)] + I_{l-1}(\mathbf{y}(\boldsymbol{\eta}, l))V(\boldsymbol{\eta}, l, \zeta), & \boldsymbol{\eta} \in \Omega_1^c \\ I_l(\boldsymbol{\eta})[1 - V(\boldsymbol{\eta}, \zeta, \zeta)] + I_{l-1}^\infty V(\boldsymbol{\eta}, \zeta, \zeta), & \mathbf{y}(\boldsymbol{\eta}, \zeta) \in \Gamma^{(L)}, \boldsymbol{\eta} \in \Omega_1^i \end{cases} \quad (4.43)$$

where  $U(\boldsymbol{\xi}, \zeta, \zeta)$  is defined by (3.21) for  $\boldsymbol{\xi} \in \Omega_l$ ,  $\zeta \in [l, \zeta]$ , and arbitrary  $\zeta_0 \in [l, \zeta]$  and  $V(\boldsymbol{\eta}, \zeta, \zeta)$  is defined by (3.21) for  $\boldsymbol{\eta} \in \Omega_{l+1}$ ,  $\zeta \in [\zeta, l+1]$ , and arbitrary  $\zeta_0 \in [\zeta, l+1]$ . For instance, for  $\nu = 0$   $\chi_l^0$  is the characteristic function for the interval  $[l, l+1]$ , and the above procedure corresponds to pairwise interpolation of the given images. When smoother trajectories and greater coupling among images are desired, higher order splines can be used in (4.39), and (3.23) or (3.28) can be solved for  $\{\mathbf{u}_l\}_{l=0}^{L-1+\nu}$  with  $\gamma = 0$  and  $Q$  replaced by  $Q^{(L)}$ .

## 5 Discretized Formulation

In this section the numerical discretization of the equations determining intensities, finite displacements and optical flows is explained. For this, let  $Q$  be divided into a grid of cells, each having dimensions  $(h, \dots, h, \tau)$ , in the  $x_1, \dots, x_N$ , and  $z$  directions, respectively, where  $h = 2^{-p}$  and  $\tau = 2^{-q}$  for positive integers  $p$  and  $q$ . Specifically, with the integer-component  $N$ -dimensional multi-indices  $\mathbf{i} = (i_1, \dots, i_N)$ ,  $\mathbf{0} = (0, \dots, 0)$ , and  $\mathbf{1} = (1, \dots, 1)$ , define the cell corners by  $(\mathbf{x}_{\mathbf{i}+1/2, z_{k+1/2}}) = (\mathbf{i}h, k\tau)$ ,  $\mathbf{0} \leq \mathbf{i} \leq 2^p \mathbf{1}$ ,  $0 \leq k \leq 2^q$ , and the cell centroids by  $(\mathbf{x}_{\mathbf{i}, z_k}) = ((\mathbf{i} - \frac{1}{2})h, (k - \frac{1}{2})\tau)$ ,  $\mathbf{1} \leq \mathbf{i} \leq 2^p \mathbf{1}$ ,  $1 \leq k \leq 2^q$ . For finite displacements  $\mathbf{x}$ , for the given images  $I_0$  and  $I_1$ , and for autonomous optical flows  $\mathbf{u}$ , only the discretization of  $\Omega$  (or  $\Omega_l$ ) is required, and  $(I_0)_{\mathbf{i}}$  for instance denotes the value of  $I_0$  at the cell centroid  $\mathbf{x}_{\mathbf{i}}$ . While the natural generalization is studied in [21], only autonomous optical flows are considered here numerically, but the corresponding intensity  $I$  is in general  $z$  dependent. Then,  $I_{\mathbf{i}, k}$  denotes the value of  $I$  at the cell centroid  $(\mathbf{x}_{\mathbf{i}, z_k})$ . Fractional indices are used for cell boundaries.

### 5.1 Intensity Discretization and Associated Integrations

First consider the intensity calculations required for finite displacements. In (3.3) multilinear interpolation of the values  $(I_0)_{\mathbf{i}}$  and  $(I_1)_{\mathbf{i}}$  is used to evaluate these intensities in the coordinates  $\mathbf{y}(\boldsymbol{\eta})$  and  $\mathbf{x}(\boldsymbol{\xi})$  respectively. In (3.3) and (3.8) the gradients  $(\nabla I_0)_{\mathbf{i}}$  and  $(\nabla I_1)_{\mathbf{i}}$  are computed at cell centers  $\mathbf{x}_{\mathbf{i}}$  by central differences with natural one-sided differences at the boundary. Then multilinear interpolation is used to evaluate the gradients  $\nabla_{\mathbf{y}} I_0$  and  $\nabla_{\mathbf{x}} I_1$  in the coordinates  $\mathbf{y}(\boldsymbol{\eta})$  and  $\mathbf{x}(\boldsymbol{\xi})$  respectively. The integrations in (3.3) and (3.8) involving intensities are computed numerically from sums of grid values at peaks of basis functions as described in detail in Subsection 7.1. The derivative  $\nabla_{\boldsymbol{\eta}} \mathbf{y}(\boldsymbol{\eta})$  is computed by central differences with natural one-sided differences at the boundary.

Now consider the intensity calculations required for optical flow. As explained in [21], in order to obtain a sufficiently accurate intensity  $I$  in each cell for the optical flow calculation, it is necessary to perform the trajectory integrations (2.20), (2.21), (3.21) and (3.22) from each cell both toward  $\Omega_0$  and toward  $\Omega_1$ . Nevertheless, a considerable savings is achieved for these integrations when the optical flow is autonomous since trajectories emanating from cells at different depths overlap in the optical flow phase space. These trajectory integrations are approximated using a Runge-Kutta method, where multilinear interpolation is used to obtain distributed values of the optical flow and its divergence. Also, optical flow derivatives are

computed using central differences, with natural one-sided differences at the boundary. The terms  $\nabla I$  and  $I_z$  are needed for the computation of optical flow in (3.24), (3.25) and (3.29), and these intensity derivatives are computed numerically as performed in [21]. Specifically,  $\nabla I$  is computed with central differences with natural one-sided modifications at the boundary. Computational experience shows that the derivative  $I_z$  is best computed from (2.10), i.e.,  $(I_z)_{i,k} = (dI/d\zeta)_{i,k} - (\nabla I)_{i,k} \cdot \tilde{\mathbf{u}}_i$ , using the most current optical flow  $\tilde{\mathbf{u}}$  and the trajectory derivative  $dI/d\zeta$  available from (3.19) or (3.20). The integrations in (3.24), (3.25) and (3.29) involving intensities are computed numerically from sums of grid values at peaks of basis functions as described in detail in Subsection 7.1.

## 5.2 Finite Element Discretization

Since only autonomous optical flows are considered here numerically, each of the boundary value problems (3.7), (3.26) and (3.28) has the form:

$$B(\boldsymbol{\varphi}, \boldsymbol{\psi}) = F(\boldsymbol{\psi}), \quad \forall \boldsymbol{\psi} \in H^\nu(\Omega, \mathbf{R}^N) \quad (5.1)$$

in which  $B$  and  $F$  possess the structure:

$$B(\boldsymbol{\psi}, \boldsymbol{\varphi}) = B(\boldsymbol{\varphi}, \boldsymbol{\psi}) = B_\mu(\boldsymbol{\varphi}, \boldsymbol{\psi}) + B_0(\boldsymbol{\varphi}, \boldsymbol{\psi}) \quad (5.2)$$

$$B_0(\boldsymbol{\varphi}, \boldsymbol{\psi}) = (\mathbf{g} \cdot \boldsymbol{\varphi}, \mathbf{g} \cdot \boldsymbol{\psi}), \quad \mathbf{g} \in L^\infty(\Omega, \mathbf{R}^N) \quad (5.3)$$

$$F(\boldsymbol{\psi}) = (\mathbf{f}, \boldsymbol{\psi})_{L^2(\Omega, \mathbf{R}^N)}, \quad \mathbf{f} \in L^2(\Omega, \mathbf{R}^N) \quad (5.4)$$

where the bilinear form  $B_0$  involves no derivatives of its arguments and the bilinear form  $B_\mu$  involves regularizing derivatives of its arguments. Furthermore, there exists a self-adjoint operator  $L$  with  $\text{Dom}(L) = H^{2\nu}(\Omega, \mathbf{R}^N)$  satisfying  $(L\boldsymbol{\varphi}, \boldsymbol{\psi})_{L^2(\Omega, \mathbf{R}^N)} = B(\boldsymbol{\varphi}, \boldsymbol{\psi})$ ,  $\forall \boldsymbol{\varphi}, \boldsymbol{\psi} \in \text{Dom}(L)$ . Because of the natural correspondence in regularity, the function space  $H^\nu(\Omega, \mathbf{R}^N)$  is approximated in the present work as well as in [20] by  $N$ -fold tensor products of B-splines of degree  $\nu$  [14],  $S_h^\nu(\Omega, \mathbf{R}^N) \subset C^{\nu-1}(\Omega, \mathbf{R}^N) \cap H^\nu(\Omega, \mathbf{R}^N)$ . However, it has been discovered recently in joint work with the authors of [17] that the lumping approach discussed below in Subsection 7.1 might be circumvented by using Lagrangian elements in a discontinuous Galerkin context, although at the expense of larger systems, and these results will be reported separately. In the proofs of Theorems 1, 2 and 3, the corresponding bilinear form  $B$  is shown to be bounded and coercive,

$$\tilde{\beta} \|\boldsymbol{\varphi}\|_{H^\nu(\Omega, \mathbf{R}^N)}^2 \leq B(\boldsymbol{\varphi}, \boldsymbol{\varphi}), \quad |B(\boldsymbol{\varphi}, \boldsymbol{\psi})| \leq \hat{\beta} \|\boldsymbol{\varphi}\|_{H^\nu(\Omega, \mathbf{R}^N)} \|\boldsymbol{\psi}\|_{H^\nu(\Omega, \mathbf{R}^N)}, \quad \forall \boldsymbol{\varphi}, \boldsymbol{\psi} \in H^\nu(\Omega, \mathbf{R}^N) \quad (5.5)$$

on  $H^\nu(\Omega, \mathbf{R}^N)$  and the corresponding linear form  $F$  is shown to be bounded on  $H^\nu(\Omega, \mathbf{R}^N)$ . Thus, (5.1) is uniquely solvable on all closed subspaces of  $H^\nu(\Omega, \mathbf{R}^N)$ , and in particular, the finite element approximation to the solution  $\boldsymbol{\varphi}$  of (5.1) is  $\boldsymbol{\varphi}_h \in S_h^\nu(\Omega, \mathbf{R}^N)$  defined by:

$$B(\boldsymbol{\varphi}_h, \boldsymbol{\chi}) = F(\boldsymbol{\chi}), \quad \forall \boldsymbol{\chi} \in S_h^\nu(\Omega, \mathbf{R}^N) \quad (5.6)$$

According to Theorems 5.1-2 and 5.2-1 of [2] the B-splines used here approximate all  $H^{2\nu}(\Omega, \mathbf{R}^N)$  functions to optimal order  $h^\nu$ . Furthermore, according to Theorems 5.1-2 and 5.2-3 of [2], the B-splines possess the additional inverse property (used to prove multigrid convergence) that their  $H^{2\nu}(\Omega, \mathbf{R}^N)$ -norm is bounded in terms of their  $L^2(\Omega, \mathbf{R}^N)$ -norm multiplied by  $h^{-\nu}$ . With optimal approximation properties, it follows with Céa's Lemma [6] that:

$$\|\boldsymbol{\varphi} - \boldsymbol{\varphi}_h\|_\nu \leq ch^\nu \|\mathbf{f}\|_{L^2(\Omega, \mathbf{R}^N)} \quad (5.7)$$

provided the solution  $\boldsymbol{\varphi}$  to (5.1) possesses the additional regularity:

$$\|\boldsymbol{\varphi}\|_{H^{2\nu}(\Omega, \mathbf{R}^N)} \leq c \|\mathbf{f}\|_{L^2(\Omega, \mathbf{R}^N)}. \quad (5.8)$$

For finite displacements, the finite element discretization outlined above is implemented in particular for (3.7) by setting  $\nu = 2$ . Then the regularity (5.8) of the solution to (3.7) follows from Theorem 2.5 of [20]. The bilinear form  $D_{\text{fd}}$  of (3.7) assumes the structure shown in (5.2), where the first term in (3.8) corresponds to  $B_\mu$  and the remaining term in (3.8) corresponds to  $B_0$ .

For the optical flow computation of (3.23), the finite element discretization outlined above is implemented by setting  $\nu = 1$ . For total variation regularization,  $\phi(s) = \mu\sqrt{s}$ , it is seen in examples of [21] that the regularity of the optical flow does not correspond to (5.8). On the other hand, for a fixed  $k$  and for a sufficiently regular  $\mathbf{u}_k$  the solution to (3.26) must possess the regularity corresponding to Gaussian regularization,  $\phi(s) = \mu s$ . For Gaussian regularization, the regularity (5.8) for solutions to (3.26) or (3.23) does not follow immediately from Theorem 2.5 of [20], but such regularity is assumed for the examples of interest in the present work. The bilinear form  $B_{\text{of},1}$  of (3.23) and (3.26) assumes the structure of (5.2), where the first integral in (3.24) (with  $\gamma = 0$ ) corresponds to  $B_0$  and the second integral of (3.24) (with integration over  $Q$  replaced by integration over  $\Omega$ ) corresponds to  $B_\mu$ .

For the optical flow computation of (3.28), the finite element discretization outlined above is implemented by setting  $\nu = 2$ . Then the regularity (5.8) of the solution to (3.28) follows from Theorem 2.5 of [20]. The bilinear form  $B_{\text{of},2}$  of (3.28) assumes the structure shown in (5.2), where the first integral in (3.29) (with  $\gamma = 0$ ) corresponds to  $B_0$  and the second integral in (3.29) (with integration over  $Q$  replaced by integration over  $\Omega$ ) corresponds to  $B_\mu$ .

## 6 Geometric Multigrid Formulation

The geometric multigrid formulation developed for (5.1) in [20] and based upon [10] is adapted here to solve the finite element discretizations of (3.7), (3.26) and (3.28). The usual multigrid strategy is generally to enhance a convergent relaxation scheme by using its initial and rapid smoothing of the smallest error scales representable on finer grids and then to transfer the problem progressively to coarser grids before relaxation is decelerated. The principal ingredients of the strategy include the definition of a smoothing relaxation scheme and the definition of a coarse grid representation of the problem which can be used to provide an improvement or correction on a finer grid.

For this, let the finest grid of  $\Omega$ , as defined in Section 5, be divided into a nested sequence of coarser grids ranging from the coarsest at level  $l = 0$  to the finest at  $l = l_{\text{max}}$ . The grid at level  $l$  consists of  $2^{p_l N}$  cells having unit aspect ratio and width  $h_l = 2^{-p_l}$  where  $p_{l+1} = p_l + 1$  and  $p_0$  is small enough that a linear system with  $N(2^{p_0} + \nu)^N$  unknowns can easily be solved directly. Thus, the cell widths on adjacent levels satisfy  $h_l = 2h_{l+1}$ . As in Section 5, the cell corners are defined in the coarse grids by  $\mathbf{x}_{i+\frac{1}{2}} = i h_l$ ,  $\mathbf{0} \leq i \leq 2^{p_l} \cdot \mathbf{1}$ , and the cell centroids by  $\mathbf{x}_i = (i - \frac{1}{2})h_l$ ,  $\mathbf{1} \leq i \leq 2^{p_l} \cdot \mathbf{1}$ . The spline basis for  $S_l^\nu(\Omega, \mathbf{R}^N) = S_{h_l}^\nu(\Omega, \mathbf{R}^N)$  is  $N(2^{p_l} + \nu)^N$ -dimensional as illustrated in Fig. 4 for  $N = 1$ ,  $\nu = 1, 2$ ,  $p_l = 1$  and  $p_{l+1} = 2$ .

Since in each case of (3.1), (3.26) and (3.28), the bilinear form of (5.1) is bounded as displayed in (5.5), the Lax-Milgram Lemma [6] guarantees the existence of an operator  $L_l$  such that:

$$(L_l \boldsymbol{\chi}, \boldsymbol{\psi})_{L^2(\Omega, \mathbf{R}^N)} = B(\boldsymbol{\chi}, \boldsymbol{\psi}), \quad \forall \boldsymbol{\chi}, \boldsymbol{\psi} \in S_l^\nu(\Omega, \mathbf{R}^N). \quad (6.1)$$

Thus, the problem (5.6) is naturally formulated on the subspaces  $S_l^\nu(\Omega, \mathbf{R}^N)$  as follows. With the  $L^2$ -projection operator  $P_l : L^2(\Omega, \mathbf{R}^N) \rightarrow S_l^\nu(\Omega, \mathbf{R}^N)$  and for  $\mathbf{f}_l = P_l \mathbf{f}$ , find  $\boldsymbol{\varphi}_l \in S_l^\nu(\Omega, \mathbf{R}^N)$  such that:

$$L_l \boldsymbol{\varphi}_l = \mathbf{f}_l, \quad \text{where} \quad L_h \boldsymbol{\varphi}_h = \mathbf{f}_h, \quad l = l_{\text{max}}. \quad (6.2)$$

Denoting by  $I_{l-1}$  the injection operator from  $(S_{l-1}^\nu(\Omega, \mathbf{R}^N), \|\cdot\|_{L^2(\Omega, \mathbf{R}^N)})$  into  $(S_l^\nu(\Omega, \mathbf{R}^N), \|\cdot\|_{L^2(\Omega, \mathbf{R}^N)})$ , the variational problems on adjacent levels can be related according to  $L_{l-1} = I_{l-1}^* L_l I_{l-1}$  [10].

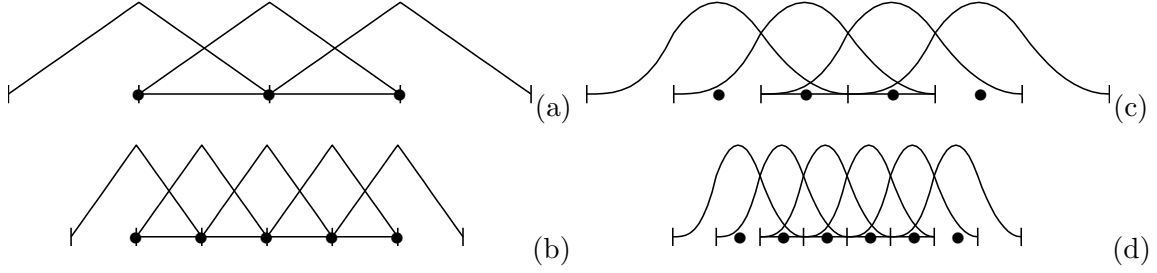


Figure 4: Examples of one-dimensional nested grids: (a)  $\nu = 1$ ,  $p = 1$ , (b)  $\nu = 1$ ,  $p = 2$ , (c)  $\nu = 2$ ,  $p = 1$ , and (d)  $\nu = 2$ ,  $p = 2$ . The horizontal line segments represent  $\Omega = (0, 1)$ , the vertical line segments denote cell boundaries, and circles mark the peaks of basis functions.

For an implementation in terms of basis function coefficients instead of on the operator level, let  $\mathbf{R}_l$  denote the  $N(2^{p_l} + \nu)^N$ -dimensional Euclidean space of basis function coefficients  $\Phi_l = \{\Phi_{l,i} \in \mathbf{R}^N : 1 \leq i \leq (2^{p_l} + \nu) \cdot \mathbf{1}\}$  for functions  $\varphi_l \in S_l^\nu(\Omega, \mathbf{R}^N)$ . Let  $K_l$  denote the bijective mapping from  $(\mathbf{R}_l, [\cdot])$  to  $(S_l^\nu(\Omega, \mathbf{R}^N), \|\cdot\|_{L^2(\Omega, \mathbf{R}^N)})$  so that  $\varphi_l = K_l \Phi_l$  holds. Also, equip  $\mathbf{R}_l$  with an  $h^\nu$ -weighted Euclidean inner product  $[\mathbf{X}_l, \mathbf{Y}_l] = h_l^N(\mathbf{X}_l, \mathbf{Y}_l)_{\ell_2}$  and inner product  $[\mathbf{X}_l] = [\mathbf{X}_l, \mathbf{X}_l]^{\frac{1}{2}}$ . Then the norms of coefficients in  $\Phi_l \in \mathbf{R}_l$  and of the corresponding functions in  $\varphi_l = K_l \Phi_l \in S_l^\nu(\Omega, \mathbf{R}^N)$  are equivalent [20]. Thus, for a basis  $\{\chi_i\}$  of  $S_l^\nu(\Omega, \mathbf{R}^N)$ , which can be expressed as  $\{K_l \mathbf{e}_i\}$  for unit vectors  $\{\mathbf{e}_i\} \subset \mathbf{R}_l$ , the coefficient matrix representations of the operators  $L_l$  are given by:

$$A_{l,ij} = (L_l \chi_i, \chi_j)_{L^2(\Omega, \mathbf{R}^N)} = (L_l K_l \mathbf{e}_i, K_l \mathbf{e}_j)_{L^2(\Omega, \mathbf{R}^N)} = [K_l^* L_l K_l \mathbf{e}_i, \mathbf{e}_j] \quad (6.3)$$

or  $A_l = K_l^* L_l K_l$ . Also the right side of (6.2) has the coefficient representation  $\mathbf{f}_l = K_l \mathbf{F}_l$  and the problem (6.2) takes the form:

$$A_l \Phi_l = \mathbf{F}_l, \quad \text{where} \quad A_h \Phi_h = \mathbf{F}_h, \quad l = l_{\max}. \quad (6.4)$$

Now the variational problems on adjacent levels are related on the coefficient space  $\mathbf{R}_l$  according to:

$$A_{l-1} = R_l^{l-1} A_l E_l^l. \quad (6.5)$$

where  $E_{l-1}^l : \mathbf{R}_{l-1} \rightarrow \mathbf{R}_l$  and its transpose  $R_l^{l-1} : \mathbf{R}_l \rightarrow \mathbf{R}_{l-1}$  are the canonical prolongation and restriction operators satisfying:

$$I_{l-1} K_{l-1} = K_l E_{l-1}^l, \quad (E_{l-1}^l)^* = R_l^{l-1} \quad (6.6)$$

In words, the relation  $I_{l-1} K_{l-1} = K_l E_{l-1}^l$  means that  $E_{l-1}^l$  produces *coefficients*  $\Phi_l = E_{l-1}^l \Phi_{l-1} \in \mathbf{R}_l$  from coefficients  $\Phi_{l-1} \in \mathbf{R}_{l-1}$  so that the *function*  $K_l \Phi_l \in S_l^\nu(\Omega, \mathbf{R}^N)$  is identical to the function  $K_{l-1} \Phi_{l-1} \in S_{l-1}^\nu(\Omega, \mathbf{R}^N)$ .

Since in each case of (3.1), (3.26) and (3.28), the bilinear form of (5.1) and (6.1) is coercive as displayed in (5.5), it follows that the symmetric matrices  $A_l$  of (6.3) are positive definite [6]. Thus, with (6.6) and (6.5) the coarse grid problem and the intergrid transfer operators have been defined. It remains to identify a suitable relaxation scheme and to define the multigrid iteration.

Since the matrices  $A_l$  are symmetric, it is natural to use a symmetric relaxation scheme. For this, the symmetric successive over-relaxation is used:

$$\Phi_l^{k+1} = S_l \Phi_l^k + \omega W_l^{-1} \mathbf{F}_l, \quad S_l = I - \omega W_l^{-1} A_l \quad (6.7)$$

where in practice  $\omega = 1$  is used in the present work. Also, the symmetric matrix  $W_l$  is given by  $W_l = (\mathcal{D}_l + \mathcal{L}_l) \mathcal{D}_l^{-1} (\mathcal{D}_l + \mathcal{L}_l^T)$  where the diagonal, strictly lower triangular and strictly upper

triangular parts of  $A_l$  are the respective terms in the sum  $A_l = \mathcal{D}_l + \mathcal{L}_l + \mathcal{L}_l^T$ . Since  $A_l$  is positive definite, it follows from  $W_l = A_l + \mathcal{L}_l \mathcal{D}_l^{-1} \mathcal{L}_l^T$  that  $W_l$  is positive definite.

This relaxation scheme is vectorized for implementation in IDL [16] by using a multi-colored ordering of cells [20] [23]. Specifically, for a stencil diameter of  $(2\nu + 1)$  a set of *same-color* cells is defined as those which are separated from one another in any of  $N$  coordinate directions by exactly  $\nu$  cells. These cells have stencils which do not weight any other cells in the set; thus, each such set of cells may be updated simultaneously in the relaxation. With this multi-colored ordering, the relaxation scheme may be implemented by performing a Jacobi iteration on same-colored cells while looping in one direction and then the other over the colors.

$$\text{for } c = 1, \dots, (\nu + 1)^N \text{ and then } c = (\nu + 1)^N, \dots, 1 \text{ do: } \Phi_l^c \leftarrow \Phi_l^c - \omega[\mathcal{D}_l^{-1}(A_l \Phi_l - \mathbf{F}_l)]^c \quad (6.8)$$

In this way, same-colored cells are updated simultaneously.

The convergence rate of the multigrid scheme depends upon the value of  $\theta$  in the following estimate:

$$[W_l] \leq (1 + \|\mathcal{D}_l^{-1} A_l\|_{\ell_\infty})[A_l] \leq \theta[A_l] \quad (6.9)$$

which is established as follows. The first inequality in (6.9) is obtained using  $W_l = A_l + \mathcal{L}_l \mathcal{D}_l^{-1} \mathcal{L}_l^T$  [20]. Since in each case of (3.1), (3.26) and (3.28), the bilinear form of (5.1) is bounded and coercive (5.5) on  $H^\nu(\Omega, \mathbf{R}^N)$ ,  $\|\mathcal{D}_l^{-1} A_l\|_{\ell_\infty}$  can be estimated as follows:

$$\begin{aligned} |D_{l,n}^{-1} A_{l,vj}| &= \left| \frac{B(\chi_i, \chi_j)}{B(\chi_i, \chi_i)} \right| \leq \frac{\hat{\beta} \|\chi_i\|_{H^\nu(\Omega, \mathbf{R}^N)} \|\chi_j\|_{H^\nu(\Omega, \mathbf{R}^N)}}{\check{\beta} \|\chi_i\|_{H^\nu(\Omega, \mathbf{R}^N)}^2} \\ &\leq \frac{\hat{\beta} \|\chi_i\|_{H^\nu(\Omega, \mathbf{R}^N)}^2 + \|\chi_j\|_{H^\nu(\Omega, \mathbf{R}^N)}^2}{2\check{\beta} \|\chi_i\|_{H^\nu(\Omega, \mathbf{R}^N)}^2} \leq \frac{\hat{\beta} \max_i \|\chi_i\|_{H^\nu(\Omega, \mathbf{R}^N)}^2}{\check{\beta} \min_i \|\chi_i\|_{H^\nu(\Omega, \mathbf{R}^N)}^2}. \end{aligned} \quad (6.10)$$

Note that the basis functions  $\{\chi_i\}$  are translation invariant and supported in  $\Omega$  in such a way that the max and min above are computed from a number of cases near  $\partial\Omega$  which depend only upon  $N$  and  $\nu$  but not  $h$  or  $l$ . Thus,  $D_{l,n}^{-1} A_{l,vj}$  is bounded independently of  $h$  and  $l$ . Note that the support of any one of the canonical B-splines of  $S_l^\nu(\Omega, \mathbf{R})$  overlaps the support of at most  $(2\nu + 1)^N$  of its translates; therefore, for the system defined on  $S_l^\nu(\Omega, \mathbf{R}^N)$ , the number of nontrivial elements in a given row of  $A_l$  is at most  $N(2\nu + 1)^N$ . With this factor times the estimate of (6.10),  $\|D_{l,n}^{-1} A_{l,vj}\|_\infty$  in (6.9) is bounded independently of  $h$  and  $l$ . Note that  $\theta$  in (6.9) depends most significantly upon  $\hat{\beta}/\check{\beta}$  in (6.10). The quotient  $\hat{\beta}/\check{\beta}$  in turn increases as the data support decreases, since the coercivity seen in (5.5) becomes ever weaker as  $\check{\beta}$  becomes ever smaller.

With the above ingredients, a symmetric two-grid cycle  $\text{TGC}(l, \sigma)$  between the finer level  $l$  and the coarser level  $l - 1$  is constructed as follows:

- 1) perform  $\sigma$  relaxation steps to update  $\Phi_l$ ,
- 2) compute the coarse-grid residual  $\mathbf{D}_{l-1} = R_{l-1}^l(\mathbf{F}_l - A_l \Phi_l)$ ,
- 3) solve the coarse grid problem  $A_{l-1} \Psi_{l-1} = \mathbf{D}_{l-1}$ ,
- 4) correct on the fine grid  $\Phi_l \leftarrow \Phi_l + E_{l-1}^l \Psi_{l-1}$ , and finally
- 5) perform another  $\sigma$  relaxation steps to update  $\Phi_l$ .

Then a symmetric multigrid cycle  $\text{MGC}(l, \sigma, \tau)$  is defined as with the two-grid cycle except that step (3) in  $\text{TGC}(l, \sigma)$  is recursively replaced with  $\tau$  iterations of  $\text{MGC}(l - 1, \sigma, \tau)$  unless for level  $l - 1 = 0$  where the coarse grid problem is solved exactly. The multigrid cycle is a  $V(\sigma)$ -cycle if  $\tau = 1$  and a  $W(\sigma)$ -cycle if  $\tau = 2$ . The nested or full multigrid iteration  $\text{FMG}(l_{\max}, \sigma, \tau)$  is given by first projecting the data to all coarse grids,  $\mathbf{F}_{l_{\max}} = \mathbf{F}$ ,  $\mathbf{F}_{l-1} = R_{l-1}^l \mathbf{F}_l$ ,  $l = l_{\max}, \dots, 1$  and solving the coarsest grid problem exactly,  $\Phi_0 = A_0^{-1} \mathbf{F}_0$ . Then with initialization  $\Phi_l = E_{l-1}^l \Phi_{l-1}$ ,  $\tau$  multigrid cycles  $\text{MGC}(l, \sigma, \tau)$  are performed up to the finest grid,  $l = 1, \dots, l_{\max}$ .

While the FMG iteration is used in practice and followed by further MGC cycles as necessary, the convergence of MGC is considered below.

The iteration matrix for the two-grid cycle can be written explicitly as:

$$M_l^{\text{TGC}}(\sigma) = S_l^\sigma [I - E_{l-1}^l A_{l-1}^{-1} R_l^{l-1} A_l] S_l^\sigma. \quad (6.11)$$

and the iteration matrix for the multigrid cycle as [10]:

$$M_l^{\text{MGC}}(\sigma, \tau) = M_l^{\text{TGC}}(\sigma) + S_l^\sigma E_{l-1}^l [M_{l-1}^{\text{MGC}}(\sigma, \tau)]^\tau A_{l-1}^{-1} R_l^{l-1} A_l S_l^\sigma. \quad (6.12)$$

The convergence framework in [10] requires to establish an approximation property and a smoothing property, which are given as follows (cf. Theorem 10.6.17, Remark 10.7.13 and Lemma 10.7.8 as well as cf. Theorem 10.7.11 in [10]):

**Theorem 4** *Under the conditions enumerated above, the following approximation property holds:*

$$0 \leq A_l^{-1} - E_{l-1}^l A_{l-1}^{-1} R_l^{l-1} \leq \theta W_l^{-1}. \quad (6.13)$$

**Theorem 5** *Under the conditions enumerated above, the smoother  $S_l$ , written in the form  $X_l = I - A_l^{1/2} S_l A_l^{-1/2} = A_l^{1/2} W_l^{-1} A_l^{1/2}$ , satisfies:*

$$0 \leq (I - X_l)^\sigma X_l (I - X_l)^\sigma \leq \eta(\sigma) I \quad (6.14)$$

where  $\eta(\sigma) = \sigma^\sigma / (1 + \sigma)^{(1+\sigma)}$  satisfies  $\lim_{\sigma \rightarrow \infty} \eta(\sigma) = 0$ .

Now (6.13) implies

$$\begin{aligned} 0 &\leq A_l^{1/2} M_l^{\text{TGC}}(\sigma) A_l^{-1/2} \\ &= [A_l^{1/2} S_l A_l^{-1/2}]^\sigma \{A_l^{1/2} [A_l^{-1} - E_{l-1}^l A_{l-1}^{-1} R_l^{l-1}] A_l^{1/2}\} [A_l^{1/2} S_l A_l^{-1/2}]^\sigma \\ &\leq [A_l^{1/2} S_l A_l^{-1/2}]^\sigma [A_l^{1/2} W_l^{-1} A_l^{1/2}] [A_l^{1/2} S_l A_l^{-1/2}]^\sigma \\ &= \theta (I - X_l)^\sigma X_l (I - X_l)^\sigma \leq \theta \eta(\sigma) I \end{aligned} \quad (6.15)$$

and thus with (6.14) the two-grid as well as the multigrid convergence are given as follows (cf. Theorem 10.7.15 and (10.7.18) in [10]):

**Theorem 6** *Under the conditions enumerated above, the two grid cycle satisfies:*

$$[A_l^{1/2} M_l^{\text{TGC}}(\sigma) A_l^{-1/2}] \leq \theta \eta(\sigma). \quad (6.16)$$

**Theorem 7** *Under the conditions enumerated above, the  $V(\sigma)$ -cycle and the  $W(\sigma)$ -cycle satisfy:*

$$[A_l^{1/2} M_l^V(\sigma) A_l^{-1/2}] \leq \frac{\theta}{\theta + \sigma}, \quad [A_l^{1/2} M_l^W(\sigma) A_l^{-1/2}] \leq \frac{\sqrt{\theta}}{\sqrt{\theta} + \sigma}. \quad (6.17)$$

## 7 Implementation Aspects

Here, implementation aspects are addressed which are not necessarily deduced from the theoretical foundation above. See also the discussion of implementation aspects in [20] which apply equally well here, including the organization of a multi-colored ordering for vectorization, the treatment of floating point errors by the careful computation of scalar products, the comparison with alternative finite difference formulations and the study of the effect of variations in data support and method parameters. The aspects considered in the subsections below deserve special treatment in the present context.

## 7.1 Lumping of Zero-Order Terms

Consider the simple case in (5.1)-(5.4) that  $N = 1$ ,  $f$  is the dotted curve in each graph of Fig. 5, and  $g$  is the characteristic function of the support of  $f$ . Solutions to (5.6) using B-

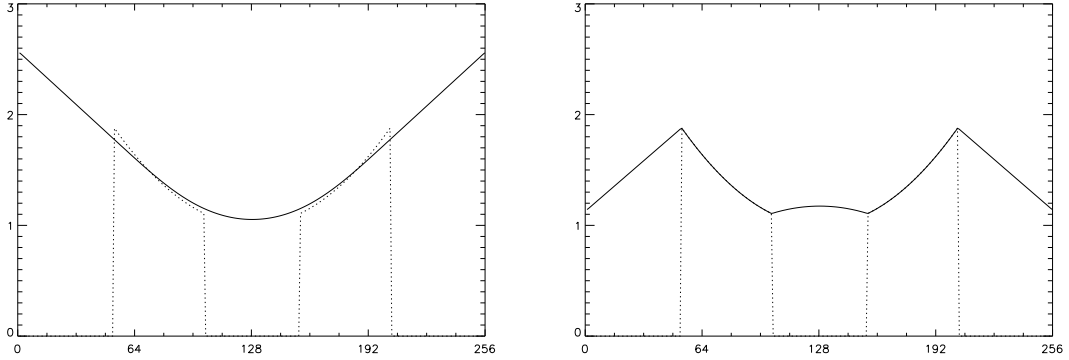


Figure 5: Solutions to (5.6) using B-splines in the pure finite element method with the cases that  $\mu$  is large and small shown respectively on the left and on the right. Here,  $N = 1$ ,  $\nu = 2$ ,  $f$  is shown in the dotted curve, and  $g$  is the characteristic function for the support of  $f$ .

splines in the pure finite element method are shown in Fig. 5 on the left and right respectively for the cases that  $\mu$  is large and small. Since the quotient  $f/g$  can be extended to an  $H^\nu(\Omega, \mathbf{R})$  function outside the data support, it can be shown there is a unique weak limit  $\varphi \in H^\nu(\Omega, \mathbf{R})$  of solutions  $\varphi^{(\mu)}$  to (5.1) as  $\mu \rightarrow 0$ . In this case,  $\varphi$  is a quadratic function satisfying  $\varphi g = f$  for noise-free data  $f$  and  $g$ . However, as seen in Fig. 5, the finite element solution  $\varphi_h^{(\mu)}$  does not converge to  $\varphi$  as  $\mu \rightarrow 0$  when the data  $g$  are discontinuous. Such convergence is of course desirable in the case of very high signal-to-noise ratios such as in this simple example. This convergence can be obtained using a lumping approach as introduced in [19]. However, as discussed in Subsection 5.2, it has been discovered recently in joint work with the authors of [17] that this lumping might be circumvented by using Lagrangian elements in a discontinuous Galerkin context, although at the expense of larger systems, and these results will be reported separately. In the lumping approach used here, the zeroth-order component of the coefficient matrix is diagonalized according to:

$$B_0(\chi_i, \chi_j) = (\mathbf{g} \cdot \chi_i, \mathbf{g} \cdot \chi_j)_{L^2(\Omega, \mathbf{R}^N)} \rightarrow \delta_{ij}(\mathbf{g}_i \cdot \mathbf{g}_i) \quad (7.1)$$

where  $\mathbf{g}_i$  denotes  $\mathbf{g}$  evaluated at basis function peaks as illustrated with the circles in Fig. 4. Specifically, the basis functions addressed in (6.3) and (7.1) are characterized as follows. Let  $\chi^\nu(\mathbf{x})$  be the canonical B-spline function of degree  $\nu$  with support in  $(\mathbf{0}, \nu + \mathbf{1})$  and peak  $\chi^\nu(\frac{1}{2}(\nu + \mathbf{1})) = 1$  whose dilation and then translations,

$$\chi_i^\nu(\mathbf{x}) = \chi^\nu(h^{-1}(\mathbf{x} - \mathbf{x}_{i - (\nu + \frac{1}{2})})), \quad \mathbf{1} \leq \mathbf{i} \leq (2^p + \nu) \cdot \mathbf{1}, \quad (7.2)$$

provide a basis for  $S_h^\nu(\Omega, \mathbf{R})$ . Then, when  $\mathbf{e}_n \in \mathbf{R}^N$  denotes the unit vector with  $\mathbf{e}_n^{(m)} = \delta_{nm}$ ,

$$\{\chi_i\} = \{\mathbf{e}_n \chi_i^\nu : \mathbf{1} \leq \mathbf{i} \leq (2^p + \nu) \cdot \mathbf{1}, \quad 1 \leq n \leq N\}. \quad (7.3)$$

Thus, when  $\chi_i = \mathbf{e}_n \chi_i^\nu$  then  $\mathbf{g}_i = \mathbf{g}(\mathbf{x}_{i - \frac{\nu}{2}})$  since  $\chi_i^\nu$  peaks at  $\mathbf{x} = \mathbf{x}_{i - \frac{\nu}{2}}$ .

With the modification shown in (7.1), convergence in the limit of increasing data fidelity and vanishing regularization is obtained as demonstrated experimentally in [19]. Furthermore, when the lumping in (7.1) is used, the grids, e.g., as illustrated in Fig. 4, can alternatively be taken to include the ghost cells situated outside  $\Omega$  in Fig. 4, the finite element coefficients  $\Phi_{h,i} = \{\Phi_{h,i}^{(n)}\} \in \mathbf{R}^N$  can be taken as solution values  $\Phi_{h,i} = \varphi_h(\mathbf{x}_{i - \frac{\nu}{2}})$  at basis function peaks

marked with circles in Fig. 4, and the numerical solution is determined pointwise as the solution to:

$$\sum_{\substack{1 \leq n \leq N \\ \mathbf{1} \leq \mathbf{j} \leq (2^p + \nu) \cdot \mathbf{1}}} \left[ B_\mu(\chi_i^\nu \mathbf{e}_m, \chi_j \mathbf{e}_n) + B_0(\chi_{i-\frac{\nu}{2}}^0 \mathbf{e}_m, \chi_{j-\frac{\nu}{2}}^0 \mathbf{e}_n) \right] \Phi_{h,\mathbf{j}}^{(n)} = F(\chi_{i-\frac{\nu}{2}}^0 \mathbf{e}_m), \quad (7.4)$$

$$\mathbf{1} \leq \mathbf{i} \leq (2^p + \nu) \cdot \mathbf{1}, \quad 1 \leq m \leq N$$

where  $B_0(\chi_{i-\frac{\nu}{2}}^0 \mathbf{e}_m, \chi_{j-\frac{\nu}{2}}^0 \mathbf{e}_n) = g_m(\mathbf{x}_{i-\frac{\nu}{2}}) g_n(\mathbf{x}_{j-\frac{\nu}{2}}) \delta_{mn}$  and  $F(\chi_{i-\frac{\nu}{2}}^0 \mathbf{e}_m) = f_m(\mathbf{x}_{i-\frac{\nu}{2}})$  follow from (5.3) and (5.4) with  $\mathbf{g}$  and  $\mathbf{f}$  extended by zero outside  $\Omega$ .

The scalar product of the left side of (7.4) with the same coefficients  $\Phi_h$  can be expressed in terms of the functions  $\varphi_h^\nu = \sum_{\mathbf{1} \leq \mathbf{i} \leq (2^p + \nu) \cdot \mathbf{1}} \Phi_{h,i} \chi_i^\nu$  and  $\varphi_h^0 = \sum_{\mathbf{1} \leq \mathbf{i} \leq (2^p + \nu) \cdot \mathbf{1}} \Phi_{h,i} \chi_{i-\frac{\nu}{2}}^0$  as  $B_\mu(\varphi_h^\nu, \varphi_h^\nu) + B_0(\varphi_h^0, \varphi_h^0)$ . Thus, the coefficient matrix in (7.4) is symmetric and non-negative. For the particular cases (3.2), (3.29) and (3.24), the coefficient matrix is shown below to be positive definite by showing that  $B_0$  is coercive on the kernel of  $B_\mu$ , where  $B_\nu$  and  $B_0$  are defined for these cases as explained at the end of Section 5.

**Theorem 8** For a given  $\mathbf{x}_k \in H^2(\Omega_0)$ , suppose that for every  $\mathbf{c} \in \mathbf{R}$  and for every matrix  $W \in \mathbf{R}^{N \times N}$  the image  $I_1$  satisfies:

$$\sum_{\mathbf{1} \leq \mathbf{i} \leq (2^p + \nu) \cdot \mathbf{1}} |\nabla_{\mathbf{x}} I_1(\mathbf{x}_k(\mathbf{x}_{i-\frac{\nu}{2}})) \cdot (\mathbf{c} + W \mathbf{x}_{i-\frac{\nu}{2}})|^2 > 0 \quad (7.5)$$

unless  $\mathbf{c} = 0$  and  $W = 0$  hold. Then the coefficient matrix  $A_{\text{fd}}$  of (7.4) corresponding to  $D_{\text{fd}}$  is symmetric and positive definite.

*Proof:* Define  $\mathbf{x}^\nu(\boldsymbol{\xi}) = \sum_{\mathbf{1} \leq \mathbf{i} \leq (2^p + \nu) \cdot \mathbf{1}} \mathbf{x}_i^* \chi_i^\nu(\boldsymbol{\xi})$  and  $\mathbf{x}^0(\boldsymbol{\xi}) = \sum_{\mathbf{1} \leq \mathbf{i} \leq (2^p + \nu) \cdot \mathbf{1}} \mathbf{x}_i^* \chi_{i-\frac{\nu}{2}}^0(\boldsymbol{\xi})$  which are in the kernels of  $B_\mu$  and  $B_0$  when  $A_{\text{fd}} \mathbf{x}^* = 0$ . Then  $\mathbf{x}^\nu$  must be an affine function of  $\boldsymbol{\xi}$  or  $\mathbf{x}_i^*$  must be an affine function of  $\mathbf{i}$ . Thus  $\mathbf{x}_i^* = \mathbf{x}^0(\mathbf{x}_{i-\frac{\nu}{2}}) = \mathbf{c} + W \mathbf{x}_{i-\frac{\nu}{2}}$  holds for a  $\mathbf{c} \in \mathbf{R}^N$  and a matrix  $W \in \mathbf{R}^{N \times N}$ . Since  $B_0(\mathbf{x}^0, \mathbf{x}^0)$  satisfies (7.5) unless  $\mathbf{x}^0 = 0$ , it follows that  $\mathbf{x}^* = 0$ . ■

**Theorem 9** Suppose that for every  $\mathbf{c} \in \mathbf{R}$  and for every skew symmetric matrix  $W \in \mathbf{R}^{N \times N}$  the intensity  $I$  satisfies:

$$\sum_{1 \leq k \leq 2^q} \sum_{\mathbf{1} \leq \mathbf{i} \leq (2^p + \nu) \cdot \mathbf{1}} |(\nabla I)_{i-\frac{\nu}{2},k} \cdot (\mathbf{c} + W \mathbf{x}_{i-\frac{\nu}{2}})|^2 > 0 \quad (7.6)$$

unless  $\mathbf{c} = 0$  and  $W = 0$  hold. Then the coefficient matrix  $A_{\text{of},1}$  of (7.4) corresponding to  $B_{\text{of},1}$  is symmetric and positive definite.

*Proof:* Define  $\mathbf{u}^\nu(\mathbf{x}) = \sum_{\mathbf{1} \leq \mathbf{i} \leq (2^p + \nu) \cdot \mathbf{1}} \mathbf{u}_i^* \chi_i^\nu(\mathbf{x})$  and  $\mathbf{u}^0(\mathbf{x}) = \sum_{\mathbf{1} \leq \mathbf{i} \leq (2^p + \nu) \cdot \mathbf{1}} \mathbf{u}_i^* \chi_{i-\frac{\nu}{2}}^0(\mathbf{x})$  which are in the kernels of  $B_\mu$  and  $B_0$  when  $A_{\text{of},1} \mathbf{u}^* = 0$ . Then  $\mathbf{u}^\nu$  satisfies  $\mathbf{u}^\nu(\mathbf{x}) = \mathbf{c} + W \mathbf{x}$  for a  $\mathbf{c} \in \mathbf{R}^N$  and a skew symmetric matrix  $W \in \mathbf{R}^{N \times N}$  [21]. Since  $\nu = 1$ ,  $\mathbf{u}_i^* = \mathbf{u}^\nu(\mathbf{x}_{i-\frac{\nu}{2}}) = \mathbf{c} + W \mathbf{x}_{i-\frac{\nu}{2}}$  holds and implies  $\mathbf{u}^0(\mathbf{x}_{i-\frac{\nu}{2}}) = \mathbf{u}_i^* = \mathbf{c} + W \mathbf{x}_{i-\frac{\nu}{2}}$ . Since  $B_0(\mathbf{u}^0, \mathbf{u}^0)$  satisfies (7.6) unless  $\mathbf{u}^0 = 0$ , it follows that  $\mathbf{u}^* = 0$ . ■

**Theorem 10** Suppose that for every  $\mathbf{c} \in \mathbf{R}$  and for every matrix  $W \in \mathbf{R}^{N \times N}$  the intensity  $I$  satisfies:

$$\sum_{1 \leq k \leq 2^q} \sum_{\mathbf{1} \leq \mathbf{i} \leq (2^p + \nu) \cdot \mathbf{1}} |(\nabla I)_{i-\frac{\nu}{2},k} \cdot (\mathbf{c} + W \mathbf{x}_{i-\frac{\nu}{2}})|^2 > 0 \quad (7.7)$$

unless  $\mathbf{c} = 0$  and  $W = 0$  hold. Then the coefficient matrix  $A_{\text{of},2}$  of (7.4) corresponding to  $B_{\text{of},2}$  is symmetric and positive definite.

Proof: Define  $\mathbf{u}^\nu(\mathbf{x}) = \sum_{\mathbf{1} \leq i \leq (2^p + \nu) \cdot \mathbf{1}} \mathbf{u}_i^* \chi_i^\nu(\mathbf{x})$  and  $\mathbf{u}^0(\mathbf{x}) = \sum_{\mathbf{1} \leq i \leq (2^p + \nu) \cdot \mathbf{1}} \mathbf{u}_i^* \chi_{i - \frac{\nu}{2}}^0(\mathbf{x})$  which are in the kernels of  $B_\mu$  and  $B_0$  when  $A_{\text{of},2} \mathbf{u}^* = 0$ . Then  $\mathbf{u}^\nu$  must be an affine function of  $\mathbf{x}$  or  $\mathbf{u}_i^*$  must be an affine function of  $i$ . Thus  $\mathbf{u}_i^* = \mathbf{u}^0(\mathbf{x}_{i - \frac{\nu}{2}}) = \mathbf{c} + W \mathbf{x}_{i - \frac{\nu}{2}}$  holds for a  $\mathbf{c} \in \mathbf{R}^N$  and a matrix  $W \in \mathbf{R}^{N \times N}$ . Since  $B_0(\mathbf{u}^0, \mathbf{u}^0)$  satisfies (7.7) unless  $\mathbf{u}^0 = 0$ , it follows that  $\mathbf{u}^* = 0$ . ■

To consider the lumping in (7.1) within the theoretical convergence framework, consider the decomposition  $L_h = L_h^\mu + L_h^0$  where  $L_h^\mu$  and  $L_h^0$  are defined as follows:

$$(L_h^\mu \chi_i, \chi_j) = B_\mu(\chi_i, \chi_j), \quad (L_h^0 \chi_i, \chi_j) = B_0(\chi_i, \chi_j) \rightarrow \delta_{ij}(\mathbf{g}_i \cdot \mathbf{g}_i) \quad (7.8)$$

where the set  $\{\chi_i\}$  is given in (7.3). Then  $L_l^\mu$  and  $L_l^0$  are defined by the Galerkin formulations,  $L_{l-1}^\mu = I_{l-1}^* L_l^\mu I_{l-1}$ ,  $L_{l-1}^0 = I_{l-1}^* L_l^0 I_{l-1}$ , for  $0 \leq l \leq l_{\max}$  and  $A_l = A_l^\mu + A_l^0$  are similarly decomposed according to (6.5) for  $0 \leq l \leq l_{\max}$ . Also,  $A_l^\mu$  is conveniently computed according to (6.3),

$$A_{l,\nu}^\mu = B_\mu(\chi_i, \chi_j) \quad (7.9)$$

while  $A_l^0$  is computed iteratively according to (6.5),

$$A_{l-1}^0 = R_l^{l-1} A_l^0 E_{l-1}^l. \quad (7.10)$$

The relations (6.6) and (6.5) hold in any case for  $A_l$ ,  $A_l^\mu$  and  $A_l^0$ . Then, instead of by (6.10),  $D_{l,\nu}^{-1} A_{l,\nu}$  is estimated as follows:

$$\begin{aligned} |D_{l,\nu}^{-1} A_{l,\nu}| &= \left| \frac{B_\mu(\chi_i, \chi_j) + \delta_{ij}(\mathbf{g}_i \cdot \mathbf{g}_i)}{B_\mu(\chi_i, \chi_i) + (\mathbf{g}_i \cdot \mathbf{g}_i)} \right| \leq \delta_{ij} + (1 - \delta_{ij}) \frac{|B_\mu(\chi_i, \chi_j)|}{B_\mu(\chi_i, \chi_i) + (\mathbf{g}_i \cdot \mathbf{g}_i)} \\ &\leq \delta_{ij} + (1 - \delta_{ij}) \frac{B_\mu(\chi_i, \chi_i) + B_\mu(\chi_j, \chi_j)}{2B_\mu(\chi_i, \chi_i)} \leq \delta_{ij} + (1 - \delta_{ij}) \frac{\max_i B_\mu(\chi_i, \chi_i)}{2 \min_i B_\mu(\chi_i, \chi_i)} \end{aligned} \quad (7.11)$$

to obtain (6.9).

## 7.2 Nonlinear Multigrid

Instead of using the lagged diffusivity iteration (3.26) as an *outer* iteration and the multigrid techniques of Section 6 as an *inner* iteration, it is natural to inquire whether these outer and inner iterations can be reversed in the usual manner of nonlinear multigrid [28]. Such an alternative formulation was tested and found to be problematic because of natural boundary conditions as explained here.

The coarse grid operator is determined naturally by (6.1) and (6.3) for the linear(ized) case. For the nonlinear case, an additional question arises concerning the representation of  $\mathbf{u}$  in the following counterpart to (6.1):

$$(L_l(\mathbf{u})\chi, \psi)_{L^2(\Omega, \mathbf{R}^N)} = B(\chi, \mathbf{u}, \psi), \quad \forall \chi, \psi \in S_l^\nu(\Omega, \mathbf{R}^N). \quad (7.12)$$

For (3.24), in particular, the question concerns the computation of  $\phi'(|\nabla \mathbf{u}^T + \nabla \mathbf{u}|^2)$  which appears as a *diffusivity* in the strong differential form of (3.23). Given a suitable approximation  $\mathbf{u}_{l+1} \in S_{l+1}^\nu(\Omega, \mathbf{R}^N)$ , the natural candidate for  $\mathbf{u}$  in (7.12) is  $\mathbf{u}_l = I_l^* \mathbf{u}_{l+1}$ . However, consider that for the 1D linear splines shown in Fig. 4, the canonical prolongation and restriction operators are given by:

$$E_l^{l-1} = \frac{1}{2} \begin{bmatrix} 2 & & & & \\ 1 & 1 & & & \\ & 2 & & & \\ & & 1 & 1 & \\ & & & & 2 \end{bmatrix}, \quad R_l^{l-1} = \frac{1}{2} \begin{bmatrix} 2 & & & & \\ & 1 & & & \\ & & 2 & & \\ & & & 1 & \\ & & & & 2 \end{bmatrix}. \quad (7.13)$$

Thus, the constant function with coefficients  $\mathbf{U}_l = \langle 1, 1, 1, 1 \rangle^T$  on the finer grid is transformed according to  $\mathbf{U}_{l-1} = R_l^{l-1} \mathbf{U}_l = \frac{1}{2} \langle 3, 4, 3 \rangle^T$  to obtain a function on the coarser grid which is not only non-constant but diminished on  $\partial\Omega$ . In general,  $\mathbf{u}_l = I_l^* \mathbf{u}_{l+1}$  is diminished on  $\partial\Omega$  in relation to  $\mathbf{u}_{l+1}$ , and thus the diffusivity obtained on level  $l$  from restriction is significantly different on the boundary than the corresponding diffusivity on level  $l+1$ . It is seen from a detailed examination of the computations that this difference corrupts the coarse grid correction of nonlinear multigrid.

While one might consider to develop an improved boundary representation of diffusivities, it is demonstrated in [28] that an outer iteration update strategy can be combined with linear multigrid in an inner iteration so that the total computational work is comparable to that of nonlinear multigrid when it functions. Such strategies can be implemented here in relation to (3.26). Nevertheless, no visible advantage to nonlinear  $\phi$  (non-constant diffusivity) could be demonstrated for practical examples in the present work, in spite of the apparent advantages evident from simple examples shown in [21].

### 7.3 Pyramidal Scheme

To accelerate the minimization of  $J_{fd}$ ,  $J_{of,1}$  and  $J_{of,2}$  a pyramidal scheme is implemented in this work as follows for a chosen  $l_{\min}$ ,  $0 \leq l_{\min} \leq l_{\max}$ , in combination with the algorithmic outline given at the end of Section 3:

- For  $l = l_{\max}, \dots, l_{\min} + 1$  restrict  $I_0$  and  $I_1$  from multigrid level  $l$  to level  $l-1$ .
- For  $l = l_{\min}, \dots, l_{\max}$ :
  - if  $l = l_{\min}$  initialize the displacement or optical flow trivially,
  - else prolong the displacement or optical flow from multigrid level  $l-1$  to level  $l$ .
  - solve for the displacement or optical flow on multigrid level  $l$ .

The efficiency of this pyramidal scheme depends upon the accurate representation of the images on the coarse grids. The example given in Subsection 7.2 shows that the images are diminished at the image domain boundary by restriction. If the restricted images are not particularly representative of those given on the fine grid, the displacement or the optical flow computed on a coarse grid may also be correspondingly biased, and the bias may draw the solution toward an undesired local minimum of the cost function on a finer grid. In such cases, stronger regularization can be used on coarser grids or else  $l_{\min}$  must be chosen nearer to  $l_{\max}$ .

## 8 Computational Results

In this final section, the numerical methods developed and analyzed in previous sections are first applied to simple test cases to demonstrate generalized rigid and generalized affine registration. A test case is also used to demonstrate the multigrid convergence guaranteed in Section 6 for each registration formulation. Then the methods are applied to realistic medical images, where generalized affine registration is intended mainly for histological applications and generalized rigid registration and interpolation are intended mainly to facilitate medical examinations by dynamic imaging.

In the test case of Fig. 6, the two given images  $I_0$  and  $I_1$  are shown respectively on the left and on the right of both of the top two rows. These images were constructed so that they may be interpolated by either an affine or by a rigid transformation. The intermediate images in the first row of Fig. 6 were interpolated by generalized affine optical flow (3.28), while the intermediate images in the second row were interpolated by generalized rigid optical flow (3.23). The successful computation of affine and rigid interpolations are evident visually from the image sequences in Fig. 6, and these results are visually independent of  $\mu$ . The

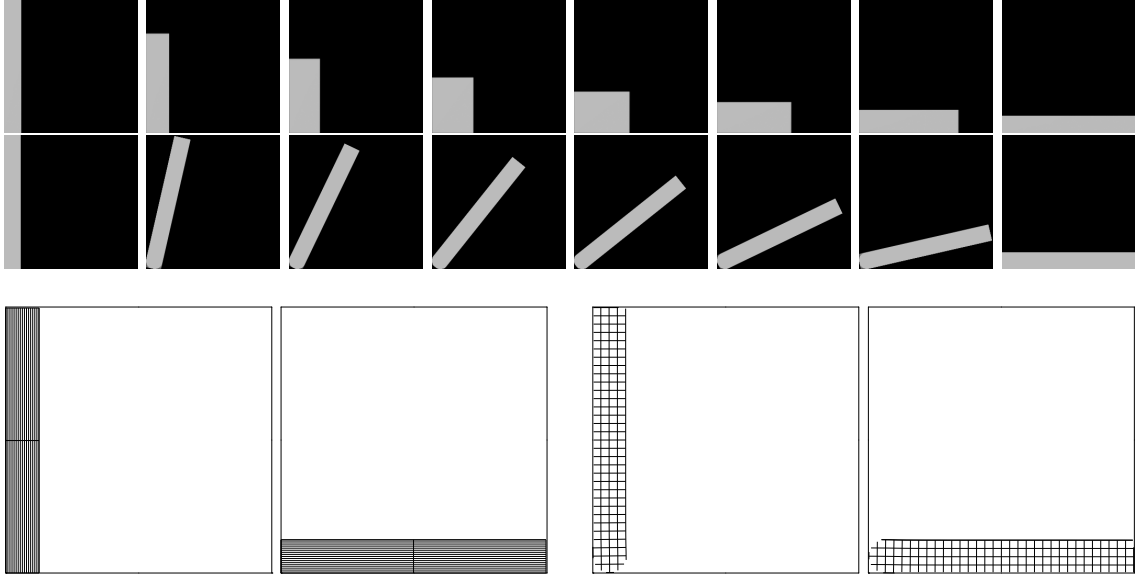


Figure 6: Interpolated image sequences obtained by generalized affine optical flow (3.28) and by generalized rigid optical flow (3.23) are shown respectively in the first and second rows. The sequences are to be read from left to right. The same images  $I_0$  and  $I_1$  were used for both sequences and are shown respectively at the left and at the right of the sequences. The registration transformations obtained are applied to a uniform grid, and the transformed grids are shown in the third row. The two transformed grids on the left were obtained by generalized affine registration, and the two transformed grids on the right were obtained by generalized rigid registration.

resulting registration transformations were applied to a uniform grid, placed first on  $\Omega_1$  and transformed to  $\Omega_0$  and then placed on  $\Omega_0$  and transformed to  $\Omega_1$ , and the transformed grids are shown in the third row of Fig. 6. The two transformed grids on the left were obtained by generalized affine registration, and the two transformed grids on the right were obtained by generalized rigid registration. Note that the generalized affine transformation compresses all grid lines in one direction while most grid lines in the other direction flow out of the domain. On the other hand, the generalized rigid transformation leaves grid lines orthogonal to one another while rotating most grid points out of the domain, including some points near the corners of the rectangular regions corresponding to nontrivial pixels in the given images. The registration errors for the generalized affine interpolation are:  $\|I_0 - \mathcal{I}_1\|_{L^2(\Omega_0, \mathbf{R})} = 0.001 = \|I_1 - \mathcal{I}_0\|_{L^2(\Omega_1, \mathbf{R})}$  and  $\|I_0 - \mathcal{I}_1\|_{L^\infty(\Omega_0, \mathbf{R})} = 0.6 = \|I_1 - \mathcal{I}_0\|_{L^\infty(\Omega_1, \mathbf{R})}$ . The registration errors for the generalized rigid interpolation are:  $\|I_0 - \mathcal{I}_1\|_{L^2(\Omega_0, \mathbf{R})} = 0.003 = \|I_1 - \mathcal{I}_0\|_{L^2(\Omega_1, \mathbf{R})}$  and  $\|I_0 - \mathcal{I}_1\|_{L^\infty(\Omega_0, \mathbf{R})} = 1.0 = \|I_1 - \mathcal{I}_0\|_{L^\infty(\Omega_1, \mathbf{R})}$ . When the given images  $I_0$  and  $I_1$  are registered according to (3.1), the morphed images  $\mathcal{I}_1$  and  $\mathcal{I}_0$  are visually indistinguishable from  $I_0$  and  $I_1$  respectively, and the registration errors are  $\|I_0 - \mathcal{I}_1\|_{L^2(\Omega_0, \mathbf{R})} = 0.004 = \|I_1 - \mathcal{I}_0\|_{L^2(\Omega_1, \mathbf{R})}$  and  $\|I_0 - \mathcal{I}_1\|_{L^\infty(\Omega_0, \mathbf{R})} = 1.0 = \|I_1 - \mathcal{I}_0\|_{L^\infty(\Omega_1, \mathbf{R})}$ .

In the test case of Fig. 7, the two given images  $I_0$  and  $I_1$  are shown respectively at the left and at the right of both rows, and these are related by an affine transformation. The intermediate images shown in the first row of Fig. 7 were interpolated by generalized affine optical flow (3.28) while those shown in the second row were interpolated by generalized rigid optical flow (3.23). The successful computation of an affine interpolation is evident visually from the sequence of images and quantitatively from the registration errors,  $\|I_0 - \mathcal{I}_1\|_{L^2(\Omega_0, \mathbf{R})} = 0.005$ ,  $\|I_0 - \mathcal{I}_1\|_{L^\infty(\Omega_0, \mathbf{R})} = 0.6$ ,  $\|I_1 - \mathcal{I}_0\|_{L^2(\Omega_1, \mathbf{R})} = 0.0$  and  $\|I_1 - \mathcal{I}_0\|_{L^\infty(\Omega_1, \mathbf{R})} = 0.0$ . The generalized affine interpolation is also visually independent of  $\mu$ . The generalized rigid interpolation is obtained using a Gaussian penalty,  $\phi(s) = \mu s$ , where  $\mu$  is large enough for the result to be strongly rigid, i.e., the resulting interpolation in the second row of Fig. 7 has the appearance of a convex combination of rigid transformations of the two images. The bias toward rigidity is evident not only visually in the image sequence but also from the larger registration errors,  $\|I_0 -$

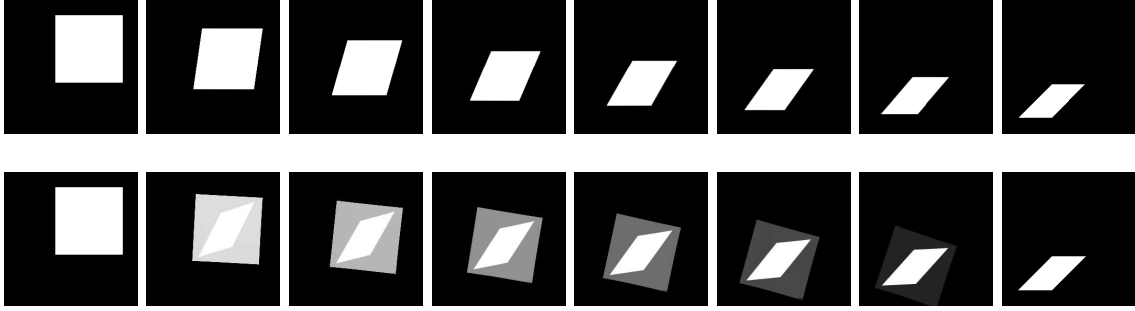


Figure 7: Interpolated image sequences obtained by generalized affine optical flow (3.28) and by generalized rigid optical flow (3.23) are shown respectively in the first and second rows. The sequences are to be read from left to right. The same images  $I_0$  and  $I_1$  were used for both sequences and are shown respectively at the left and at the right of the sequences.

$\mathcal{I}_1\|_{L^2(\Omega_0, \mathbf{R})} = 0.18$ ,  $\|I_0 - \mathcal{I}_1\|_{L^\infty(\Omega_0, \mathbf{R})} = 1.0$ ,  $\|I_1 - \mathcal{I}_0\|_{L^2(\Omega_1, \mathbf{R})} = 0.17$  and  $\|I_1 - \mathcal{I}_0\|_{L^\infty(\Omega_1, \mathbf{R})} = 1.0$ . When the given images  $I_0$  and  $I_1$  are registered according to (3.1), the morphed images  $\mathcal{I}_1$  and  $\mathcal{I}_0$  are visually indistinguishable from  $I_0$  and  $I_1$  respectively, and the registration errors are  $\|I_0 - \mathcal{I}_1\|_{L^2(\Omega_0, \mathbf{R})} = 0.005$ ,  $\|I_0 - \mathcal{I}_1\|_{L^\infty(\Omega_0, \mathbf{R})} = 0.5$ ,  $\|I_1 - \mathcal{I}_0\|_{L^2(\Omega_1, \mathbf{R})} = 0.0003$  and  $\|I_1 - \mathcal{I}_0\|_{L^\infty(\Omega_1, \mathbf{R})} = 0.4$ .

The computations described above were carried out as outlined in Subsection 7.3 with reference to the algorithmic outline given at the end of Section 3. In particular,  $2^p = 256$ ,  $l_{\max} = 5$ ,  $l_{\min} = 0$  and  $\mu/h^{2\nu} = 10^5$  were used and MGC-V(1) iterations were performed for each level of the pyramidal scheme. In each case, many outer iterations were performed on the coarser pyramidal levels where they are inexpensive, and then only a few outer iterations were performed on the finer pyramidal levels. For the final outer iteration on the finest pyramidal level, graphical representations of the convergence of MGC-V(1) iterations for (3.1), (3.23) and (3.28) for the example of Fig. 7 are shown in Fig. 8 by plotting on a  $\log_{10}$ -scale the differences

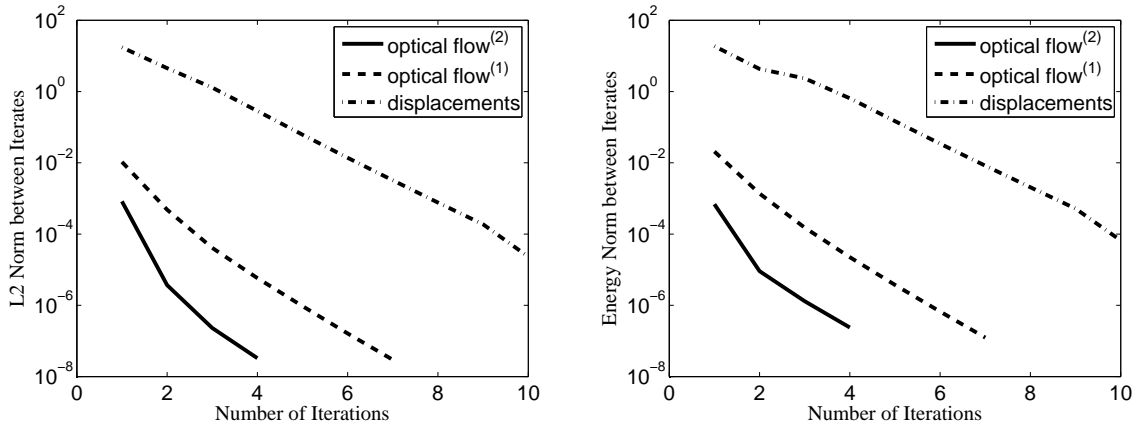


Figure 8: Convergence histories for (3.1), (3.23) and (3.28) of  $e_h^k = \Phi_h^k - \Phi_h^{k-1}$  are shown here for MGC-V(1) iterations (a) in the norm  $\|e_h^k\|_{\ell_2}$  on the left and (b) in the norm  $\|A_h^{1/2} e_h^k\|_{\ell_2}$  on the right. The solid curve is for (3.28), the dashed curve is for (3.23), and the dot-dashed curve is for (3.1).

$e_h^k = \Phi_h^k - \Phi_h^{k-1}$  as functions  $\|e_h^k\|_{\ell_2}$  and  $\|A_h^{1/2} e_h^k\|_{\ell_2}$  of iteration number  $k$ . The multigrid reduction factors  $\rho^{(k)} = \|A_h^{1/2} e_h^k\|_{\ell_2} / \|A_h^{1/2} e_h^{k-1}\|_{\ell_2}$  are  $\rho^{(3)} = 0.14$  for (3.28),  $\rho^{(5)} = 0.17$  for (3.23), and  $\rho^{(9)} = 0.25$  for (3.1). The smaller multigrid reduction factors for optical flow can be understood from the fact that the data  $\int_0^1 \nabla I(\mathbf{x}, z) \nabla I(\mathbf{x}, z)^T dz$  for optical flow have broader support than the data  $\nabla I_1(\mathbf{x}) \nabla I_1(\mathbf{x})^T$  for finite displacements; thus, for optical flow the quotient  $\hat{\beta}/\beta$  in (6.10) is smaller and consequently  $\theta$  in (6.9) is smaller. See also the related experiments in [20].

In the example of Fig. 9, a sequence of images,  $I_0$ ,  $I_1$ ,  $I_1 \circ \mathbf{x}_1$  and  $I_2$  from histological sections

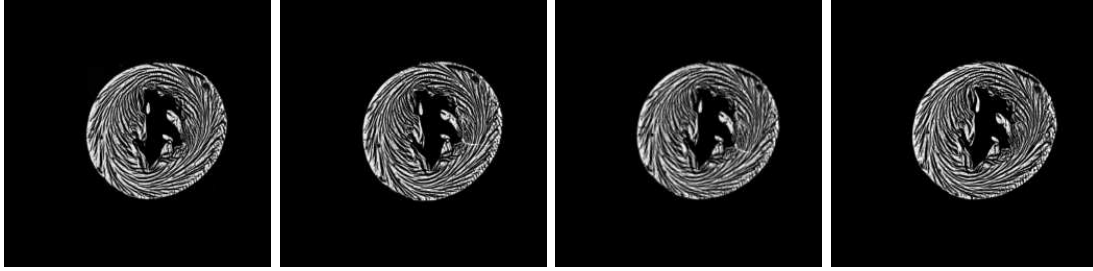


Figure 9: Images  $I_0$ ,  $I_1$ ,  $I_1 \circ \mathbf{x}_1$  and  $I_2$  from histological sections of a mouse heart are shown from left to right, where the image  $I_1 \circ \mathbf{x}_1$  is registered to  $I_0$  and  $I_2$ .

of a mouse heart is shown, where the image  $I_1 \circ \mathbf{x}_1$  is registered to  $I_0$  and  $I_2$  by minimizing (4.36) with  $L = 2$  and with frozen end transformations  $\mathbf{x}_0(\boldsymbol{\xi}) = \boldsymbol{\xi}$  and  $\mathbf{x}_2(\boldsymbol{\xi}) = \boldsymbol{\xi}$ . Again,  $2^p = 256$ ,  $l_{\max} = 5$ ,  $l_{\min} = 0$ ,  $\mu/h^{2\nu} = 10^5$  and MGC- $V(1)$  iterations were used. As mentioned in Section 1, generalized affine registration is suitable for histological applications because sections may be affine deformed in the process of slicing. On the other hand, without fixing certain images in (4.36), (generalized) affine transformations can expand or contract images so that an object is deformed essentially to the same size throughout the entire stack. This effect can also be controlled by the number of updates performed in order to solve the entire coupled optimality system for (4.36). The effect may be controlled more rigorously by incorporating additional penalties on volume changes, but this goal is achieved by generalized rigid registration [3]. The three raw images in Fig. 9 are actually one triple taken from a lengthy sequence of histological sections of a mouse heart, such as used in [3], and the raw and registered sequences are shown in 3D in Fig. 10, where the sequence registration is performed by first shifting all images to the same center of mass and then proceeding with finite displacements as described in Section 4. Films of the raw and registered sequences can be viewed by downloading them respectively from:

<http://math.uni-graz.at/invcon/medimage/histofilm1.mpg>  
<http://math.uni-graz.at/invcon/medimage/histofilm2.mpg>

In the example of Fig. 11, respiratory motion accompanies the sudden and widespread appearance of contrast agent, particularly in the kidneys, and it is required to interpolate between the two given images shown respectively at the left and at the right. The other images shown in the figure have been interpolated using generalized rigid optical flow; in fact, the scaling function approach of [18] is used to treat the appearance of contrast agent. Again,  $2^p = 256$ ,  $l_{\max} = 5$ ,  $l_{\min} = 0$ ,  $\mu/h^{2\nu} = 10^5$  and MGC- $V(1)$  iterations were used. The soft tissues move as a result of respiration but the spinal column, for instance, remains rigid. Such an example appears to be a good candidate for a realistic application of total variation regularization as discussed in [21]. However, as indicated in Subsection 7.2, the result shown in Fig. 11 is not perceptibly affected by the use of total variation regularization. The raw and interpolated images shown in Fig. 11 are actually samples taken from a lengthy temporal sequence in which temporal resolution is low enough for the raw sequence to be quite jerky but high enough to permit a smooth interpolation which facilitates the medical examination. The raw image sequence has been interpolated pairwise using generalized rigid optical flow, and the raw and interpolated films can be viewed by downloading them respectively from:

<http://math.uni-graz.at/invcon/medimage/respfilm1.mpg>  
<http://math.uni-graz.at/invcon/medimage/respfilm2.mpg>

## References

- [1] R.A. ADAMS, *Sobolev Spaces*, Academic Press, New York, 1975.

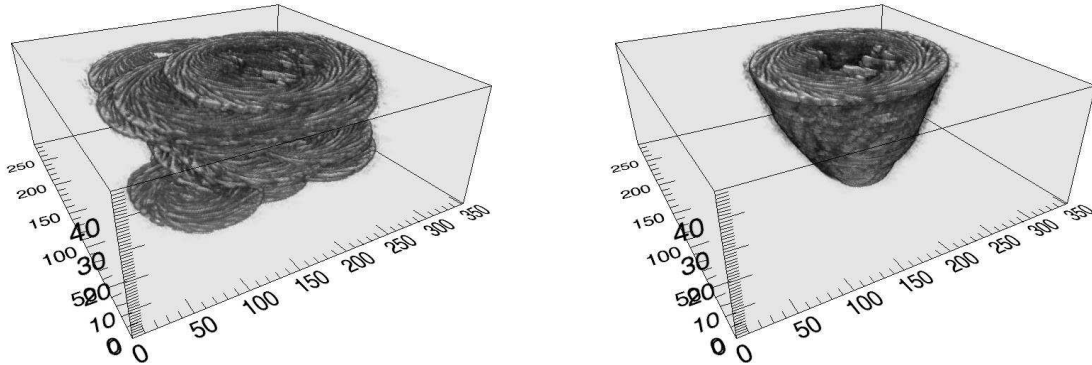


Figure 10: A sequence of histological sections of a mouse heart are shown unregistered on the left and registered by finite displacements on the right.

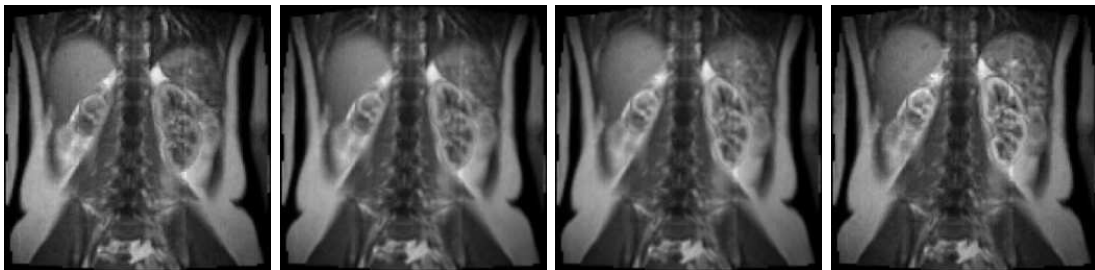


Figure 11: The two given images  $I_0$  and  $I_1$  are shown on the left and right respectively. The intermediate images have been interpolated by generalized rigid optical flow.

- [2] J. AUBIN, *Approximation of Elliptic Boundary-Value Problems*, Krieger, Huntington, New York, 1980.
- [3] R. BURTON, G. PLANK, J. SCHNEIDER, A.J. PRASSL, J. LEE, V. GRAU, N. SMITH, N. TRAYANOVA, P. KOHL, H. AHAMMER and S.L. KEELING, *3-Dimensional Models of Individual Cardiac Histo-Anatomy: Tools and Challenges*, to appear in the Annals of the New York Academy of Sciences.
- [4] D.R.J. CHILLINGWORTH, *Differential Topology with a View to Applications*, Pitman, London, 1976.
- [5] G.E. CHRISTENSEN, H.J. JOHNSON, *Consistent Image Registration*, IEEE Trans. Med. Imaging. Vol. 20, No. 7, July 2001, pp. 568-582.
- [6] P.G. CIARLET, *The Finite Element Method for Elliptic Problems*, North-Holland, Amsterdam, 1978.
- [7] B. FISCHER, J. MODERSITZKI, *Curvature Based Image Registration*, J. Math. Imaging and Vision 18, pp. 81-85, 2003.
- [8] B. FISCHER, J. MODERSITZKI, *Fast Inversion of Matrices Arising in Image Processing*, Numerical Algorithms 22, pp. 1-11, 1999.
- [9] L. GARCIN and L. YOUNES, *Geodesic Image Matching: A Wavelet Based Energy Minimization Scheme*, EMMCVPR, 2005.
- [10] W. HACKBUSCH, *Iterative Solution of Large Sparse Systems of Equations*, Springer, 1993.

- [11] S. HAKER, A. TANNENBAUM, and R. KIKINIS, *Mass Preserving Mappings and Image Registration*, MICCAI 2001, pp. 120–127.
- [12] S. HENN, *A Multigrid Method for a Fourth-Order Diffusion Equation with Application to Image Processing*, SIAM J. Sci. Comput. (SISC), Vol. 27, No. 3, pp. 831–849, 2005.
- [13] S. HENN and K. WITSCH, *Iterative Multigrid Regularization Techniques for Image Matching*, SIAM J. Sci. Comput. (SISC), Vol. 23, No. 4, pp. 1077–1093, 2001.
- [14] K. HÖLLIG, *Finite Element Methods with B-Splines*, Frontiers in Applied Mathematics 26, SIAM, 2003.
- [15] B.K.P. HORN and B.G. SCHUNCK, *Determining Optical Flow*, Artif. Intell., Vol. 23, pp. 185 – 203, 1981.
- [16] IDL: <http://www.itlvis.com/idl/>.
- [17] O. KARAKASHIAN and T.D. KATSAOUNIS, *A discontinuous Galerkin Method for the Incompressible Navier-Stokes Equations*, Proceedings of the International Symposium on the Discontinuous Galerkin Method, B. Cockburn, G.E. Karniadakis, C-W. Shu (eds). Springer Lecture Notes in Computational Science and Engineering 11, pp. 157–166, 2000.
- [18] S.L. KEELING, *Image Similarity Based on Intensity Scaling*, to appear in J. Math. Imaging and Vision.
- [19] S.L. KEELING and R. BAMMER, *A Variational Approach to Magnetic Resonance Coil Sensitivity Estimation*, Appl. Math. Comp., Vol. 158, pp. 359–388, 2004.
- [20] S.L. KEELING and G. HAASE, *Geometric Multigrid for High-Order Regularizations of Early Vision Problems*, Appl. Math. and Comp., Vol. 184, pp. 536–556, 2007.
- [21] S.L. KEELING and W. RING, *Medical Image Registration and Interpolation by Optical Flow with Maximal Rigidity*, J. Math. Imag. Vision, Vol. 23, No. 1, pp. 47–65, July 2005.
- [22] MATLAB: <http://www.mathworks.com>.
- [23] G. MEURANT, *Computer Solution of Large Linear Systems*, Elsevier, New York, 1999.
- [24] J. MODERSITZKI, *FLIRT with rigidity - image registration with a local non-rigidity penalty*, IJCV, pp. 1–18, 2007.
- [25] J. MODERSITZKI, *Numerical Methods for Image Registration*, Oxford University Press, 2004.
- [26] W. PECKAR, C. SCHNÖRR, K. ROHR, H.S. STIEHL, *Parameter-Free Elastic Deformation Approach for 2D and 3D Registration using Prescribed Displacements*, J. Math. Imaging and Vision, Vol. 10, pp. 143–162, 1999.
- [27] D. RUECKERT, L.I. SONODA, C. HAYES, D.L.G. HILL, M.O. LEACH and D.J. HAWKES, *Non-rigid Registration using Free-Form Deformations: Application to Breast MR Images*, IEEE Trans. Med. Imaging, Vol. 18, No. 8, pp. 712–721, 1999.
- [28] U. TROTTEBERG, C. OOSTERLEE, and A. SCHÜLLER, *Multigrid*, Academic Press, San Diego, San Francisco, New York, Boston, London, Sydney, Tokyo, 2001.
- [29] C.R. VOGEL and M.E. Oman, *Iterative Methods for Total Variation Denoising*, SIAM Journal on Scientific Computing, Vol. 17, pp. 227–238, 1996.